TURUN
YLIOPISTO
Matemaattis-luonnontieteellinen
tiedekunta

In situ U-Pb zircon age determination on plagioclase porphyry dike from Siilinjärvi

Vilma Hurttila

Geologia
Pro gradu -tutkielma
Laajuus: 30 op

27.5.2025
Turku

Master's thesis

Subject: Bedrock Geology
Author: Vilma Hurttila
Title: In situ U-Pb zircon age determination on plagioclase porphyry dike from Siilinjärvi
Supervisors: Esa Heilimo, Teemu Vehkamäki
Number of pages: 65 pages + 3 appendices
Date: 27.5.2025

U-Pb isotopic dating provides a reliable method to determine the timing of magmatic and metamorphic events. Zircon is an ideal mineral for U-Pb geochronology due to its durability and uranium-accommodating crystal structure. Finnish Precambrian bedrock records a long and complex geological history, with the boundary between the Archean Karelia Province and the Svecofennia Province providing valuable insights into crustal evolution processes. The Siilinjärvi carbonatite Complex, located within the Archean rocks of eastern Finland near the Svecofennian boundary, represents one of the world's oldest carbonatites (~2.61 Ga). Understanding the timing and nature of later magmatic events in the region is crucial for interpreting the complex crustal evolution involving Archean structures and Proterozoic overprinting. This study focuses on determining the crystallization age of a plagioclase porphyry dike from the Siilinjärvi apatite mine, interpreted as the youngest magmatic phase in the immediate area. The aim is to determine the emplacement age of this dike and to understand its genesis and implications for the geological evolution of the region.

In situ U-Pb geochronology was performed on zircons extracted from the plagioclase porphyry dike using LA-ICPMS. Detailed petrographic studies using optical microscopy and whole-rock geochemical analyses were conducted on the porphyry dike and three comparative rock samples from the Muuruvesi suite. The U-Pb dating of the plagioclase porphyry yielded a concordia age of 1900 ± 14 Ma from analyses of the outermost zircon rims. The zircon population was complex, also containing abundant older, inherited Archean cores (predominantly 2.5−2.8 Ga) and a Paleoproterozoic age population (2.07−2.30 Ga). Geochemically, the plagioclase porphyry is distinct from the Muuruvesi suite samples, characterized by higher alkali content (Na_2O+K_2O). In contrast, the Muuruvesi suite samples are geochemically similar to quartz-diorites, tonalites and granodiorites used as a reference group from the area. All investigated samples display significant low-grade metamorphic alteration features, including sericitization, saussuritization, and the formation of epidote-group minerals and chlorite. The plagioclase porphyry exhibits additional replacement of plagioclase by K-feldspar and calcite.

The 1900 ± 14 Ma age obtained for the plagioclase porphyry is interpreted in two ways: it may represent Svecofennian crystallization age, supported by magmatic zoning in zircon rims and temporal alignment with Svecofennian collisional events. Alternatively, it could record Svecofennian metamorphic overprint on an older intrusion as suggested by the upper intercept of a discordia line at 2584 ± 27 Ma and the low Th/U ratios (0.026–0.072) in the youngest zircon rims, which are characteristic of metamorphic zircon. Further research specifically U-Pb crystallization dating of the Muuruvesi suite samples, is essential to resolve the emplacement age of the plagioclase porphyry dike and to provide more understanding of the Svecofennian orogenic events and their impact on the Siilinjärvi area.

Key words: U-Pb dating, zircon, plagioclase porphyry, Siilinjärvi, geochemistry

Pro gradu -tutkielma

Pääaine: Kallioperägeologia
Tekijä: Vilma Hurttila
Otsikko: In situ U-Pb zirkoni-iänmääritys Siilinjärven plagioklaasiporfyyrijuonesta
Ohjaajat: Esa Heilimo, Teemu Vehkamäki
Sivumäärä: 65 sivua + 3 liitettä
Päivämäärä: 27.5.2025

U-Pb isotooppi-ikämääritysmenetelmä on luotettava tapa määrittää magmaattisten ja metamorfisten tapahtumien ajankohta. Zirkoni on erinomainen mineraali U-Pb geokronologiassa sen kestävyyden sekä uraania sitovan kiderakenteen vuoksi. Suomen kallioperällä on pitkä ja monimutkainen geologinen historia ja arkeeisen Karjalan provinssin sekä Svekofennian provinssin välinen raja tarjoaa arvokasta tietoa kuoren kehitysprosesseista. Siilinjärven karbonatiittikompleksi, joka sijaitsee Itä-Suomen arkeeisella kallioperällä lähellä Svekofennian rajaa, edustaa yhtä maailman vanhimmista karbonatiiteista (n. 2,61 Ga). Myöhempien magmaattisten tapahtumien ajoituksen ja luonteen ymmärtäminen on tärkeää tulkittaessa monimutkaista kuoren kehitystä, johon liittyy arkeeisia rakenteita ja proterotsooista uudelleenmuokkausta. Tämä tutkimus keskittyy Siilinjärven apatiittikaivoksella sijaitsevan plagioklaasiporfyyrijuonen kiteytymisiän määrittämiseen, jonka tulkitaan olevan lähialueen nuorin magmaattinen vaihe. Tavoitteena on määrittää juonen intruusioikä sekä ymmärtää sen syntyä ja merkitystä alueen geologiselle kehitykselle.

Plagioklaasiporfyyrijuonesta erotetuille zirkoneille tehtiin in situ U-Pb-geokronologinen ajoitus käyttäen LA-ICPMS-menetelmää. Juonelle ja kolmelle vertailtavalle mikrotonaliittiselle Muuruveden sarjan kivinäytteille tehtiin petrografiset tutkimukset optisella mikroskopialla sekä kokokivigeokemialliset analyysit. Plagioklaasiporfyyrin U-Pb-ajoitus tuotti zirkonien uloimmilta reunoilta analysoidun konkordia-iän 1900 ± 14 Ma. Zirkonipopulaatio oli monimutkainen, sisältäen myös runsaasti vanhempia, perittyjä arkeeisia ytimiä (pääasiassa 2,5–2,8 Ga) sekä paleoproterotsooisen ikäryhmän (2,07–2,30 Ga). Geokemiallisesti plagioklaasiporfyyri eroaa Muuruveden sarjan näytteistä korkeamman alkalipitoisuutensa (Na_2O+K_2O) perusteella. Sen sijaan Muuruveden sarjan näytteet ovat geokemiallisesti samankaltaisia alueen vertailuryhmänä käytettyjen kvartsidioriittien, tonaliittien ja granodioriittien kanssa. Kaikissa tutkituissa näytteissä on havaittavissa merkittäviä matalan asteen metamorfisia muuttumispiirteitä, kuten serisiittiytymistä, saussuriittiytymistä sekä epidoottiryhmän mineraalien ja kloriitin muodostumista. Plagioklaasiporfyyrissä esiintyy lisäksi plagioklaasin korvautumista kalimaasälvällä sekä kalsiittia.

Plagioklaasiporfyyrille saatua 1900 ± 14 Ma:n ikää voidaan tulkita kahdella tavalla: se voi edustaa svekofennistä kiteytymisikää, mitä tukevat zirkonien reunojen magmaattiset kasvuvyöhykkeet ja ajallinen yhteys svekofennisiin orogeenisiin tapahtumiin. Vaihtoehtoisesti ikä voi kuvastaa svekofennistä metamorfista vaikutusta vanhempaan intruusioon, mitä tukee diskordian ylempi leikkauspiste 2584 ± 27 Ma:ssa sekä nuorimpien zirkonireunojen matalat Th/U-suhteet (0,026–0,072), jotka ovat tyypillisiä metamorfisille zirkoneille. Jatkotutkimukset, erityisesti Muuruveden sarjan näytteiden U-Pb-kiteytymisikien ajoittaminen, olisivat tärkeitä plagioklaasiporfyyrijuonen iän selvittämiseksi ja Siilinjärven alueen svekofennisten orogeenisten tapahtumien ja niiden vaikutusten tarkemmaksi ymmärtämiseksi.

Avainsanat: U-Pb-ikämääritys, zirkoni, plagioklaasi porfyyri, Siilinjärvi, geokemia

Contents

1 Introduction

Geochronological and geochemical methods are valuable in understanding the evolution of the continental crust. U-Pb zircon dating, especially when applied to zircon, is a reliable technique for determining the timing of magmatic and metamorphic events due to zircon's durability and ability to incorporate uranium and exclude initial lead (Faure 1977; Finch and Hanchar 2003). When combined with petrographic and whole-rock geochemical data, these methods help to understand the origin, evolution and timing of geological processes (Jara et al. 2021).

The Precambrian rocks of Finland, part of the Fennoscandian Shield, have formed through complex geological processes involving multiple orogenic events, crustal reworking, and extensive metamorphic and magmatic activity over billions of years. It can be broadly divided into two main regions. The northern and eastern areas are characterized by Archean rocks, over 2.5 Ga old, while southern and central Finland are dominated by Paleoproterozoic Svecofennian rocks, dated to ca. 1.93−1.80 Ga (Vaasjoki et al., 2005). The Karelia province has experienced crustal extension and rifting, involving periods of mafic magmatism and dike emplacement (∼2.5−2.44 Ga), resulting in continental breakup around 2.06 Ga (Lahtinen et al. 2005; Vuollo and Huhma 2005).

Within the Archean rocks of central eastern Finland lies the Siilinjärvi carbonatite Complex, considered one of the oldest known carbonatites in the world, with an age of approximately 2.61 Ga (O'Brien et al. 2005). It has experienced complex geological evolution, including metamorphism and intrusions by younger magmatic rocks (O'Brien et al. 2015). Understanding the magmatic history and the relationships between different intrusives within and around the Complex is essential for interpreting the broader crustal evolution of the region.

The aim of this study is to determine the crystallization age of a plagioclase porphyry dike sampled from Siilinjärvi apatite mine using in situ U-Pb zircon geochronology. In addition, the petrography and whole-rock geochemistry of the dike and three rock samples, part of Muuruvesi suite, from the area are examined and compared to reference data. By combining geochronological, geochemical and petrographic data this study investigates the origin and evolution of the studied dike and its implications for the crustal development in the Siilinjärvi area.

2 The U-Pb dating method

2.1 Fundamentals of radioactive decay and its role in geochronology

When unstable atoms undergo spontaneous transformations in the nuclei, involving emission of particles and radiant energy, the process is known as radioactivity (Faure 1977). The rate at which nuclei decay over time remains proportional to the total number of nuclei present at any given moment, occurring independently of external factors (Allègre 2008). This relationship can be expressed by the equation:

$$\frac{dN}{dt} = -\lambda N \tag{1}$$

where N is the number of radioactive nuclei at a given time, λ is the decay constant, which defines the probability of decay per unit time, and dN/dt represents the rate of change in the number of nuclei. The negative sign indicates that the number of parent nuclei decreases over time as they undergo radioactive decay (Dickin 2018). The equation 1 can be solved to give the equation:

$$N = N_0 e^{-\lambda t} \tag{2}$$

where N_0 is the initial number of radioactive nuclei at time $t = 0$. It shows the amount of parent isotopes N that remain at any time t out of the original number of nuclei N_0 (Faure 1977). The decay constant λ is related to the half-life $t_{1/2}$ of the parent isotope, giving the time it takes half of the parent isotope to decay. This relationship can be shown as $\lambda = \frac{ln2}{t_{1/2}}$.

The decay of a radioactive parent isotope results in the formation of radiogenic daughter isotopes. Daughter isotopes formed can be calculated from $D^* = N_0 - N$ (Faure 1977). Assuming no daughter isotopes were lost, added or present at $t = 0$, the quantity of radiogenic daughter isotopes D^* at any given time t, forming from the decay of parent isotopes, can be calculated from equation:

$$D^* = N_0(1 - e^{-\lambda t}) \quad (3)$$

The total number of daughter isotopes D includes both the radiogenic daughter isotopes D^* and any initial daughter isotopes D_0. The total number can be calculated from $D = D_0 + D^*$. (Faure 1977). It can be more beneficial to replace N_0 with $Ne^{\lambda t}$ in equation 3, as the total number of daughter isotopes D and the number of parent isotopes remaining N can be measured when making age determinations from minerals. We can then obtain equation:

$$D = D_0 + N(e^{\lambda t} - 1) \quad (4)$$

This equation expresses the total amount of daughter isotopes at time t, incorporating both the contribution from the initial daughter isotopes D_0 and the newly formed daughter isotopes from the decay of the parent isotopes. The equation 4 can be solved for t, to calculate the age of a rock or a mineral, if the rock or mineral have stayed as a closed system, so neither parent or daughter isotope have been lost or gained, the decay constant λ and the initial number of D_0 is known accurately and the D and N measurements are correct (Faure 1977).

The three naturally occurring isotopes of uranium are ^{238}U, ^{235}U and ^{234}U, all of them being radioactive. ^{238}U decays to stable ^{206}Pb and ^{235}U decays to stable ^{207}Pb through a particular decay chain, which is visualized in Figure 1. Alpha decay is spontaneous emission of alpha particles from nuclei. The emission of an alpha particle, which is consisted of two protons and two neutrons, produces daughter isotope, which mass number is reduced by four. Through alpha decay the daughter isotopes of ^{238}U and ^{235}U are ^{234}Th and ^{231}Th (Faure 1977).

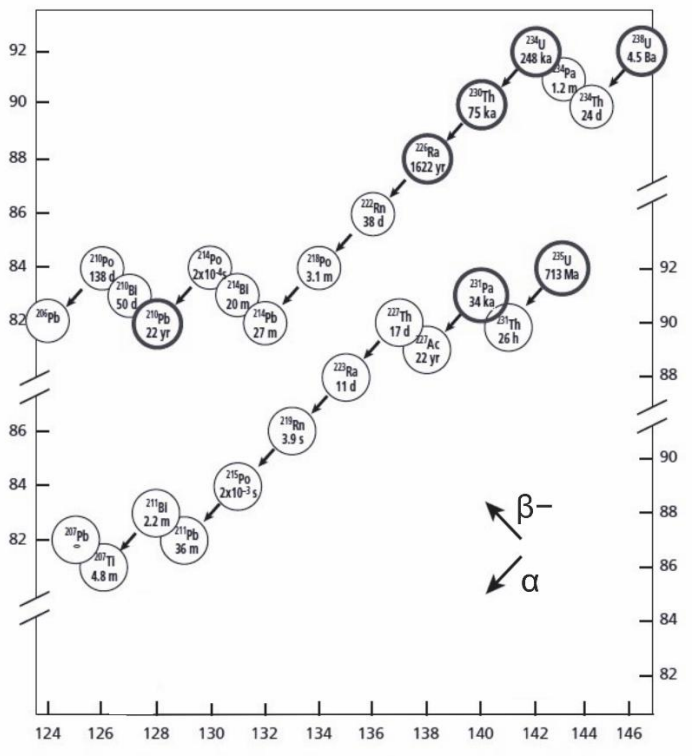

Figure 1. Decay chain series of ^{235}U and ^{238}U. Modified after Allègre (2008).

Unstable atoms can undergo beta decay, taking the form as either beta-minus (β^-) or beta-plus (β^+) decay. In beta-minus decay, a neutron in the nucleus transforms into a proton, and an electron, known as the negative beta particle, is emitted. As a result of this process, the atomic number increases by one, and the number of neutrons is decreased by one, leaving the mass number unchanged. After uranium has decayed to ^{234}Th and ^{231}Th through alpha decay, the thoriums undergo beta-minus decay, resulting in ^{234}Pa and ^{231}Pa. The decay chain from ^{238}U to ^{206}Pb includes eight alpha particles and six beta particle emissions in total and several intermediate daughter isotopes with branching. The decay of ^{235}U to ^{207}Pb works in a similar manner but requires only seven alpha particles and four beta particle emissions. The intermediate daughter isotopes of these decay chains differ from each other, as ^{238}U produces uranium series intermediate daughter isotopes, and ^{235}U produces actinium series intermediate daughter isotopes. The ^{235}U and ^{238}U have significantly longer half-lives compared to the half-lives of their intermediate daughter isotopes. As a result, their decay chains eventually reach secular equilibrium, where the rate at which new daughter isotopes are produced equals the rate at which they decay. If system has remained closed, secular equilibrium ensures that the production of the final stable isotope occurs at the same rate as the decay of the original uranium isotope (Faure 1977).

Benefit of using the uranium-lead system for dating is the presence of the two independent decay chains (Corfu 2015). The natural abundance of ^{238}U, ^{235}U and ^{234}U are 99.2739 %, 0.7204 % and 0.0057 %, respectively. Lead occurs naturally as four different stable isotopes, ^{208}Pb, ^{207}Pb, ^{206}Pb and ^{204}Pb. Out of the four lead isotopes, only ^{204}Pb is non-radiogenic, making it suitable for use as a reference isotope, even though it is weakly radioactive, with a half-life of approximately $1.4 * 10^{17}$ years (Faure 1977).

The two uranium isotopes decay at different rates, producing two independent age estimates for the same sample. Despite their significantly different decay constants, both uranium and lead isotopes share similar chemical properties (Faure 1977; Allègre 2008). If the two ages are the same, making them concordant, it confirms that the mineral has acted as a closed system, with no loss or gain of uranium or lead since its formation (Allègre 2008; Corfu 2015). However, if the ages differ, giving discordant results, it indicates that the system was open at some point (Corfu 2015). For reliable age determination, the following criteria should ideally be met: The mineral must have stayed closed, ensuring that uranium, lead and their intermediate daughters were neither lost nor added during its history. The initial lead isotope ratios and the decay constants for ^{238}U and ^{235}U must be known correctly. Results must be precise without errors, and the composition of uranium must be normal. This would give concordant ages. However, in practice, most minerals do not remain perfectly closed systems, leading to discordant ages due to the loss or gain of uranium or lead (Faure 1977).

Concordia diagram is a graphical method used in U-Pb geochronology to evaluate whether a mineral has remained a closed system or has experienced open-system behavior due to lead loss or gain. Concordia curve can be constructed by plotting the ratio of ^{207}Pb/^{235}U on the x-axis and ^{206}Pb/^{238}U on the y-axis using equations $x = (e^{\lambda 235t} - 1)$ and $y = (e^{\lambda 238t} - 1)$. If a mineral has remained closed the two independent U-Pb ages should be concordant, and the data point will fall on the concordia curve. (Allègre 2008). When a uranium-bearing mineral crystallizes, it essentially contains no radiogenic lead, plotting at the origin of the concordia diagram. Over time, if the system remains closed, the isotopic ratios will evolve along the concordia curve as radiogenic lead accumulates. If the system has opened and has experienced loss of lead or gain of uranium, the isotopic ratios will plot off the concordia curve giving discordant dates. In cases of lead loss, data

points typically form a linear trend, called the discordia line, which intersects the concordia curve at two points (Faure 1977). The upper intercept of this line, T_0, represents the crystallization age of the mineral, while the lower intercept, T_1, may correspond to the time of lead loss, often caused by metamorphism or fluid alteration (Faure 1977; Allègre 2008). If the system loses more lead than uranium, the data points will fall between the ages T_1 and T_0, whereas if uranium loss is greater than lead loss, the points will shift above the expected age, placing them above the concordia curve (Allègre 2008). This concordia diagram was introduced by Wetherill (1956), as a graphical method for evaluating U-Pb isotopic data (Schoene 2013). Wetherill concordia diagram can be seen in Figure 2. Tilton (1960) proposed that Pb loss could also occur through continuous diffusion within the crystal lattice rather than a single discrete event. This explained how Pb loss in zircon could happen gradually over time, leading to curved discordia instead of the expected straight lines from episodic Pb loss (Faure 1977; Schoene 2013).

Figure 3 presents the Tera-Wasserburg (T-W) diagram, which provides a different representation to the Wetherill concordia diagram. Instead of plotting the conventional $^{206}Pb/^{238}U$ and $^{207}Pb/^{235}U$ ratios as in the Wetherill diagram, the T-W diagram uses $^{238}U/^{206}Pb$ on the x-axis and $^{207}Pb/^{206}Pb$ on the y-axis. This enables the identification of both concordant and discordant data similarly to the Wetherill method (Schoene 2013). The T-W diagram allows for the analysis of samples with high initial lead content, even when the isotopic composition of that lead is unknown. In such cases, the data points can align along an isochron. The point where this isochron intersects the $^{207}Pb/^{206}Pb$ axis represents the initial lead composition, while the point where it intersects the concordia curve corresponds to the sample's formation age (Reiners et al. 2017).

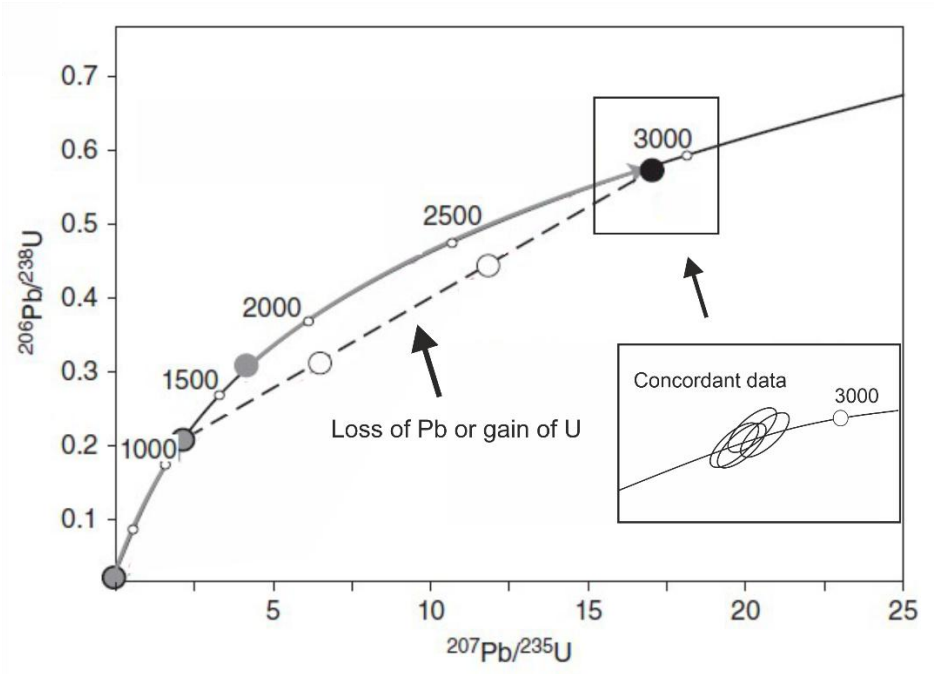

Figure 2. Wetherill concordia diagram. Concordant points plot along the concordia curve, representing systems that remained closed since crystallization. Lead loss can cause the points to plot off the concordia, and discordia line can be formed where the intercepts indicate the timing of crystallization and the lead loss event. Inset demonstrates concordant data and timing of crystallization. Modified after Reiners et al. (2017).

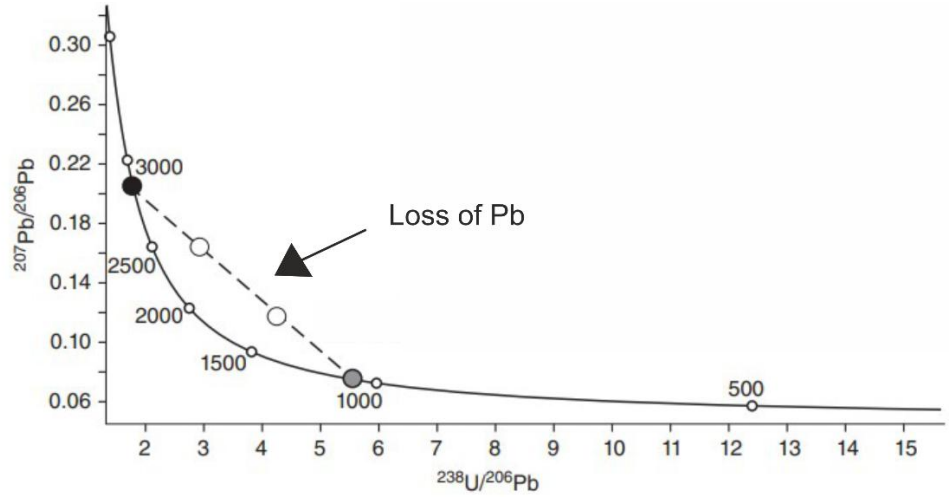

Figure 3. Tera-Wasserburg diagram. Concordant points plot along concordia curve, discordant points form discordia line. Modified after Reiners et al. (2017).

The isotopic composition and accumulation of radiogenic lead isotopes in uranium-bearing minerals, can be determined using the following equations:

$$\frac{^{206}Pb}{^{204}Pb} = \left(\frac{^{206}Pb}{^{204}Pb}\right)_0 + \frac{^{238}U}{^{204}Pb}\left(e^{\lambda_{238}t} - 1\right) \quad (5)$$

$$\frac{^{207}Pb}{^{204}Pb} = \left(\frac{^{207}Pb}{^{204}Pb}\right)_0 + \frac{^{235}U}{^{204}Pb}(e^{\lambda_{235}t} - 1) \quad (6)$$

where $\left(\frac{^{207}Pb}{^{204}Pb}\right)_0$ represents the initial lead isotope ratios at the time of formation. These equations can be used to plot $^{206}Pb/^{204}Pb$ and $^{238}U/^{204}Pb$ isochron diagram (Faure 1977). The calculated data can display a linear trend on the isochron diagram (Figure 4), which strongly suggests that the samples share a common initial lead isotopic composition, where its slope equals to $e^{\lambda_{238}t} - 1$, and the y-axis intercept gives the initial lead isotope ratio (Schoene 2013; Dickin 2018).

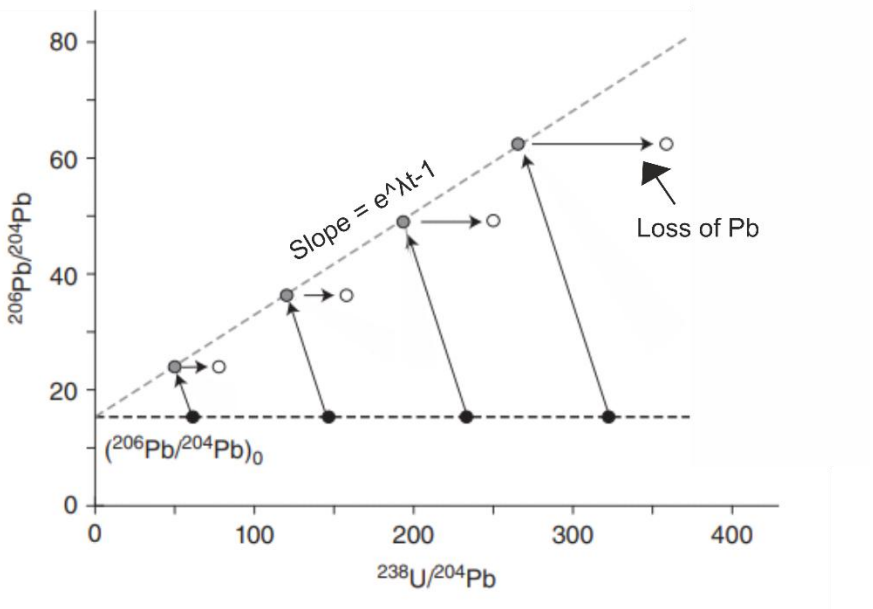

Figure 4. U-Pb isochron diagram exhibiting cogenetic samples with similar $^{206}Pb/^{204}Pb$ composition at the time of crystallization. The slope represents the amount of radiogenic lead accumulated at time. Lead loss lowers the measured ratios, reducing the slope of array and leading to apparent younger age. Modified after Reiners et al. (2017).

While U-Pb isochron dating requires that the system remained closed to both uranium and lead, Pb-Pb isochron dating is less affected by uranium loss because it relies only on lead isotope ratios. This makes it useful for samples where uranium may have been mobilized, as long as lead isotopes remained undisturbed. The Pb-Pb dating equation to show $^{207}Pb/^{206}Pb$ ratio is derived by combining equations 5 and 6 (Faure 1977).

$$\frac{\frac{^{207}Pb}{^{204}Pb} - \left(\frac{^{207}Pb}{^{204}Pb}\right)_0}{\frac{^{206}Pb}{^{204}Pb} - \left(\frac{^{206}Pb}{^{204}Pb}\right)_0} = \frac{^{235}U}{^{238}U}\left[\frac{e^{\lambda_2 t} - 1}{e^{\lambda_1 t} - 1}\right] = \left(\frac{^{207}Pb}{^{206}Pb}\right)^* \quad (6)$$

Here $(\frac{207Pb}{206Pb})^*$ is radiogenic isotope ratio (Schoene 2013). This equation assumes that the $^{235}U/^{238}U$ ratio is constant and equals to $1/137.8$, and concentration of uranium can then be neglected (Faure 1977). Because the Pb-Pb dating method relies only on lead isotope ratios and does not require uranium concentration measurements, it is particularly valuable for samples that have experienced alteration that may have affected uranium concentration (Dickin 2018). The Pb-Pb method helps to minimize challenges caused by open-system behavior (Faure 1977). The Pb-Pb system still relies on the assumption of closed-system behavior since the time of formation, up until the time of analysis, excluding recent alterations like chemical weathering (Dickin 2018).

2.2 Zircon

The most used mineral for U-Pb dating method is zircon. Zircon ($ZrSiO_4$) is commonly found in igneous, metamorphic and sedimentary rocks as an accessory mineral. Zircon is an orthosilicate and has tetragonal crystal structure with Zr^{4+} and Si^{4+} cations (Finch and Hanchar 2003). The ionic radius of zirconium is 0.84 Å and uranium is 1.00 Å. The zirconium in zircons can therefore often be replaced by uranium, as their ionic radius is similar, and uranium also occurs in tetravalent oxidation state (U^{4+}) (Faure 1977; Finch and Hanchar 2003). Lead has larger ionic radius (1.32 Å) and lower charge and is therefore not notably included in zircon at the time of formation (Faure 1977). One of zircon's strengths is also its exceptional durability and resistance to geological processes, such as metamorphism and surface weathering that typically break down other minerals (Finch and Hanchar 2003).

Zircon typically forms tetragonal, prismatic crystals, with elongation that is controlled primarily by crystallization velocity. Figure 5 shows shapes of some zircons obtained from a rock from Siilinjärvi. Faster cooling in volcanic and shallow intrusions results in needle-like crystals, while slower cooling in deep-seated intrusions produces equant or stubby forms. Other factors influencing zircon morphology include magma composition and crystallization temperature (Corfu et al. 2003).

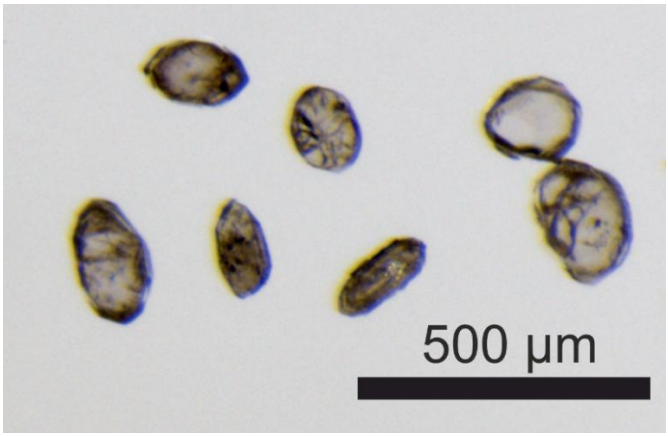

Figure 5. Zircons from Siilinjärvi area (EPHE-2015-301.1) The zircon grains are mostly subhedral to euhedral exhibiting some prismatic and bipyramid shapes. Some are more rounded and stubbier and internal fractures are visible.

A key characteristic of magmatic zircon is growth zoning, which is best observed using cathodoluminescence (CL) or backscattered electron (BSE) imaging. These patterns can be seen in Figure 6. Internal structures of igneous zircons can be observed from BSE and CL imaging because of heterogeneous distribution of elements (Corfu et al. 2003). Other main features found in igneous zircons are oscillatory and sector zoning (Hoskin and Schaltegger 2003). The zoning in zircon reflects variations in the concentrations of zirconium and silicon, as well as significant differences in trace elements like hafnium, yttrium, phosphorus, REEs, uranium, and thorium (Corfu et al. 2003). These compositional variations typically range between two, one of which is nearly pure zircon with very low trace-element content, while the other exhibits high enrichment in trace elements, with impurities constituting a few percent of the total weight (Speer 1982). Growth zoning forms as a result of periodic changes during crystal development. It is influenced by factors such as the phase of crystal formation, the characteristics of the interface between the crystal and melt, melt supersaturation levels, oxidation conditions and diffusion behavior. Final phases of magmatic crystallization can also affect zircon growth. One common alteration occurs in the later stages of magmatic cooling and after the magma has solidified, where concentric oscillatory zoning in magmatic zircon is disrupted. One typical feature is the appearance of irregular, homogeneous regions with low uranium content, which cut across the pre-existing growth zones. These regions can be formed through recrystallization, resulting in a zircon composition that becomes closer

to pure zircon while impurities are concentrated into complex, trace-element-rich zones (Corfu et al. 2003).

Figure 6. CL images showing magmatic growth zoning patterns in zircons from typical crustal rocks. Relatively simple and fine bands with alternating bright and dark luminescence. Scale bars approximately 50 μm. Modified after Corfu et al. (2003).

In zircon affected by metamictization, zoning may also be visible under a microscope. Due to its wider variability in intensity range of emissions, CL imaging is usually more effective compared to BSE imaging in identifying distinct growth zones within zircon. BSE imaging highlights differences in mean atomic number of areas within a material, like zircon. Areas with higher atomic numbers reflect more electrons and appear brighter in the image (Corfu et al. 2003). In cathodoluminescence images areas with lower uranium contents appear as bright zones, and darker areas contain higher amounts of uranium (Corfu 2015).

Many igneous rocks contain xenocrystic zircon, which originates from pre-existing zircon that was incorporated into the magma. These xenocrysts may appear as cores surrounded by recently formed zircon overgrowths or as isolated, partially rounded crystals. Identifying xenocrystic cores can be easier when the contrast in the amount of uranium across the core and outer rim is high. High-U cores undergo metamictization, causing them to expand and develop distinct pink, brown to opaque colouration. In the case where

there is much uranium in the core and not in the rim, the core can expand and lead to fracturing of the rim. In contrast, higher U content in the rim leads to darkening over time but it generally does not fracture (Corfu et al. 2003).

Metamictization occurs in zircon as radioactive decay of uranium causes damage to the crystal lattice. Over time, the accumulation of radiation damage lowers zircon's density and produces other physical and optical alterations. As zircons are composed of zones of varying uranium concentrations, the zones with high uranium concentration expand and apply stress, leading to fracturing in the uranium-poor layers (Corfu 2015). These fractures typically radiate outward from high-U inclusions to low-U zones. Fracture patterns caused by metamictizations can be seen in Figure 7. The fracture systems are controlled by factors such as metamictization degree, "shell" thickness and external pressure (Corfu et al. 2003). These fractures create pathways for fluids to enter, leading to chemical changes, including the leaching of lead and the introduction of elements such as iron and calcium (Corfu et al. 2003; Corfu 2015). Since uranium tends to remain within the undamaged portions of the crystal lattice, it is less likely to be lost compared to lead. Complex zoning patterns can complicate dating processes, especially when the analysis involves mixed ages from different zones, which may be further affected by lead loss, adding additional uncertainty (Corfu 2015).

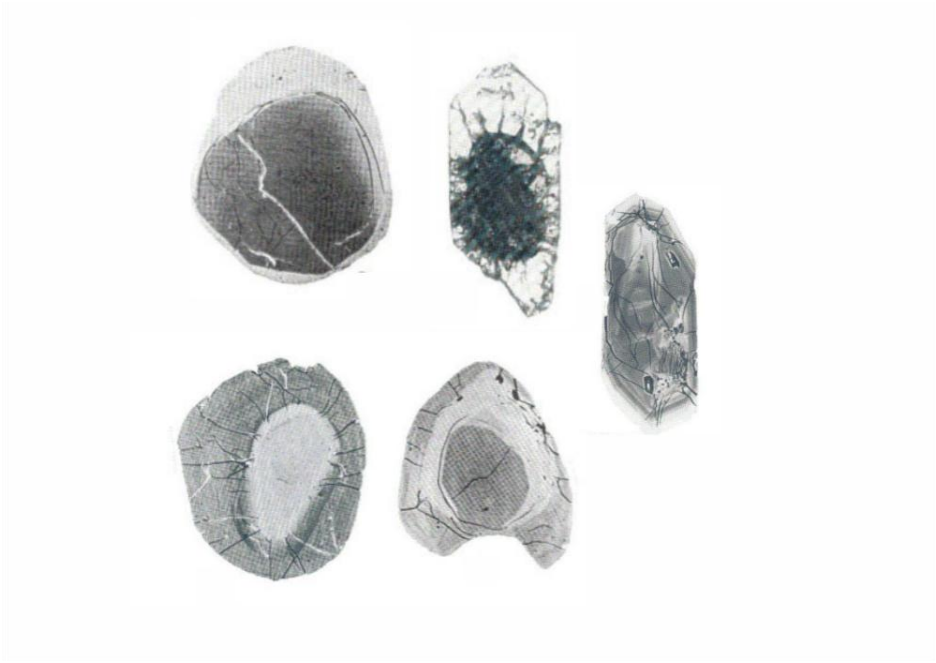

Figure 7. BSE and transmitted light images of metamict zircons and their resulting fracture patterns. U-rich areas (lighter parts) cause expansion and fracturing to the lower uranium areas of the grain. Zircon sizes are between 70-250 µm. Modified after Corfu et al. 2003.

3 Regional geology

3.1 Fennoscandian shield

The East European Craton extends across northern and eastern Europe as well as northwestern Russia (Vaasjoki et al. 2005). The East European craton consists of the crustal segments of Fennoscandia, Volgo-Uralia and Sarmatia (Figure 8; Nironen 2017). Fennoscandian shield may be distinguished into Svecofennia, Sveconorwegia, Karelia, Lapland-Kola and Norrbotten Provinces, while it excludes Caledonides in Norway, Sweden and in part of Finland (Vaasjoki et al. 2005; Nironen 2017). The Precambrian rocks of Finland consist of Archean rocks, Paleoproterozoic rocks and younger rock formations, such as Rapakivi granites (Vaasjoki et al. 2005).

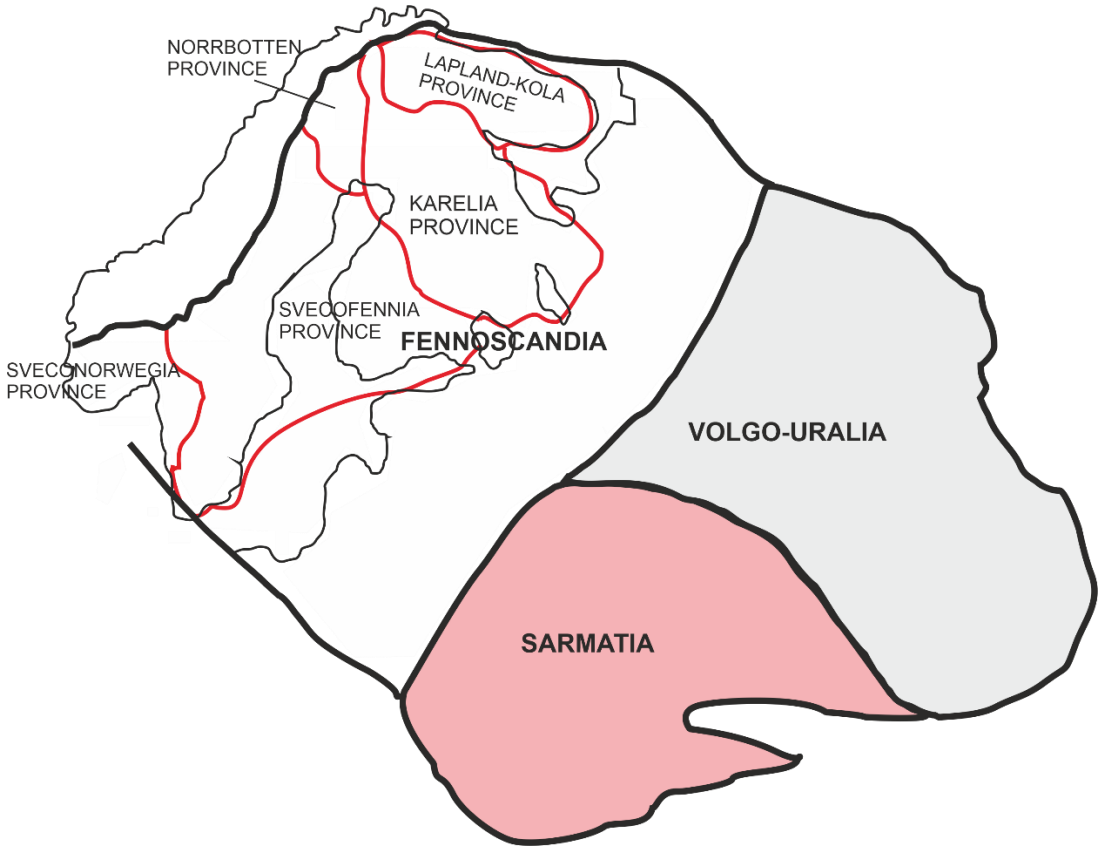

Figure 8. East-European craton, crustal segments of Fennoscandia, Volgo-Uralia and Sarmatia. Fennoscandian shield and the Provinces within, modified after Gorbatschev and Bogdanova (1993) as well as Nironen (2017).

3.2 Formation of Archean rocks

The Archean rocks of Finland are located in the eastern and northern parts of Finland and were formed between approximately 3.5 and 2 billion years ago. They consist mainly of granite gneiss-greenstone terranes and is divided into the Kola and Karelia Provinces. The Karelia Province is represented by greenstone belts, ages ranging from 2.94 to 2.74 Ga (Hölttä et al. 2012), and metasedimentary belts, with over twenty greenstone belts bordered by Archean rocks such as tonalites, trondhjemites, granodiorites, and granites. These belts exhibit a distinct north-south linear trend (Gaál and Gorbatschev 1987; Sorjonen-Ward and Luukkonen 2005). The granitoids of the Karelia Province can be classified into four major groups: TTG (tonalite-trondhjemite-granodiorite), sanukitoids, quartz diorite, quartz monzodiorite, and granodiorite-granite-monzogranite (Hölttä et al. 2012). The TTGs of the Archean were formed between 3.5 and 2.73 Ga. Plutonic rocks within the Archean rocks, including sanukitoids, quartz diorites, and granites, formed between 2.74 and 2.66 Ga (Nironen 2017).

The current structure of the Karelia Province was shaped by a series of geological events. During the Neoarchean, accretionary processes between 2.83 and 2.75 Ga led to the formation of the Province, followed by crustal thickening through collisional processes, occurring between 2.73 and 2.68 Ga (Hölttä et al. 2012). In addition, the structure was influenced by the collision between Kola and Karelia Provinces as well as Archean rifting (Sorjonen-Ward and Luukkonen 2005). The Siilinjärvi carbonatite Complex, dated approximately 2.6 Ga, represents one of the Archean-age intrusions (O'Brien et al. 2005). These structures were later significantly modified during the Svecofennian orogeny (Hölttä et al. 2012).

3.3 Rifting of Archean craton

Shear zones in the Karelia Province, primarily oriented north-south, likely formed during the assembly of Archaean terranes and subsequently reactivated during episodes of crustal extension, as evidenced by the Siilinjärvi carbonatite, likely emplaced in a Neoarchaean rift, providing evidence of these processes and is now bounded by Palaeoproterozoic shear zones (Nironen 2017).

The Paleoproterozoic rifting of the stabilized Archean crust began with the formation of layered mafic intrusions around 2.5–2.44 Ga indicating the start of Archean crustal rifting. Additional evidence of periodic crustal extension comes from mafic magmatic activity dated to 2.3 Ga, 2.2 Ga, 2.1 Ga, and 2.05 Ga, forming intrusions, sills, and dike swarms. Several NW-, E-, and NE- dike swarms crosscut the whole Archean craton (Vuollo and Huhma 2005). The period of the Archean rifting lasted from 2.5 to 2.1 Ga, resulting to the continental breakup at around 2.06 Ga (Lahtinen et al. 2005).

The Paleoproterozoic sedimentary rocks known as the Karelian formations (2.5–1.9 Ga), and volcanic rocks, such as Koivusaari volcanite (~2.0 Ga) were deposited and erupted on the Archean basement, reflecting a transition in the depositional setting from rifting to continental breakup (Kontinen et al. 1992; Laajoki 2005; Nironen 2017). Some quartzites and arkoses in the northern part of the craton have possibly formed during Neoarchean, indicating that first extensional rift basins might have begun developing on the Neoarchaean crust around 2.6–2.5 Ga (Nironen 2017).

3.4 Svecofennian orogen

The arc-complexes of Svecofennian orogeny are Western Finland Subprovince and Southern Finland Subprovince. The Svecofennia Province in Finland includes several terranes, including Vaasa Complex, Central Finland Granitoid Complex, Savo Belt, and Tampere- , Häme- , Pirkanmaa- and Uusimaa belt (Figure 9; Nironen 2017).

The Svecofennia Province, south of the Karelia Province, consists of only Paleoproterozoic rocks, and is separated from the Karelia Province by Raahe-Ladoga Shear Complex (Kärki et al. 1993; Abdel Zaher et al. 2017). Oblique convergence of microcontinent and Karelia caused NW-SE trending and approximately 100 km wide zone of strongly sheared rocks (Kärki et al. 2012; Abdel Zaher et al. 2017). These structures developed over an extended period through multiple phases of the Svecofennian convergence. The shear-dominated structures within the Raahe-Ladoga Shear Complex are composed of metamorphosed supracrustal rocks, specifically paragneisses, along with intrusive rocks (Kärki et al. 2012).

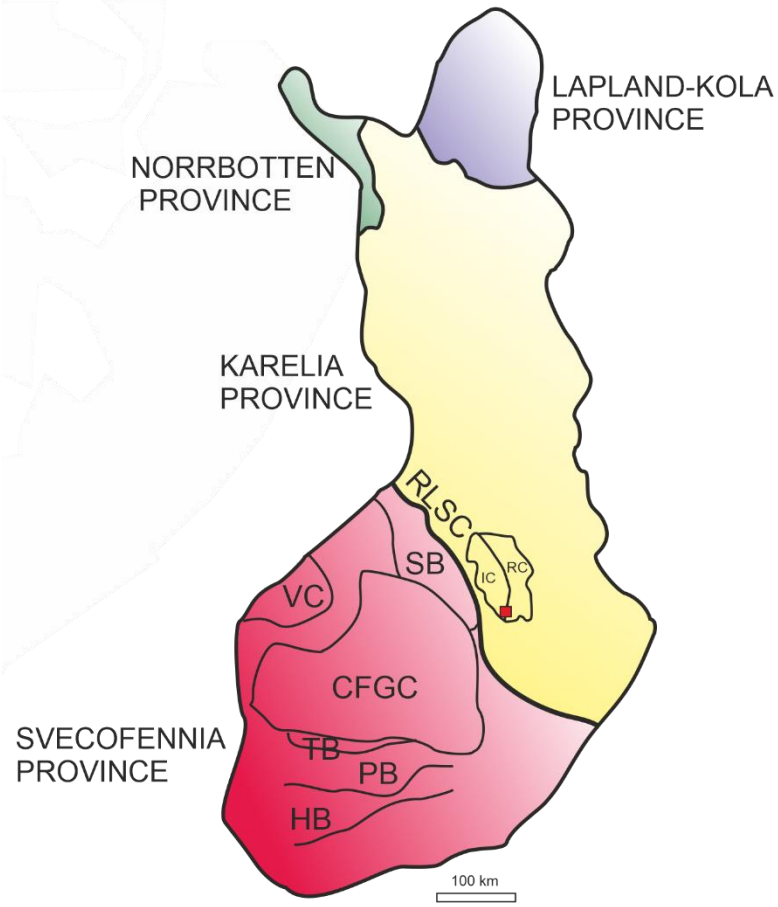

Figure 9. Simplified map of Finland with Provinces and terranes within. Siilinjärvi located with red box. RLSC = Raahe-Ladoga Shear Complex, IC = Iisalmi Complex, RC = Rautavaara Complex, SB = Savo Belt, VC = Vaasa Complex, CFGC = Central Finland Granitoid Complex, TB = Tampere Belt, PB = Pirkanmaa Belt, HB = Häme Belt. Modified after Nironen (2017).

Five overlapping orogenies can be considered to have contributed to the formation of Svecofennian orogeny, which shaped the Svecofennia Province, through multi-stage accretions and collisions of microcontinents and island-arcs. This includes microcontinent accretion, between 1.92 and 1.88 Ga, crustal extension during 1.87–1.84 Ga, continent-continent collision from 1.87 to 1.79 Ga, and gravitational collapse between 1.79 and 1.77 Ga (Korja et al. 2006).

The accretion of Svecofennian microcontinents began with the collisions of Kola and Karelia Provinces around 1.93 Ga, during which subduction was occurring southwestward beneath the Lapland-Kola region, leading to the formation of a back-arc basin. The collision reached closure by 1.91 Ga, which was proceeded with collision of microcontinent and Karelia Province at 1.92–1.89 Ga. A significant north-south collision occurred between 1.89 and 1.87 Ga, which led to the accretion of microcontinent and

island arc. A new collision in the south formed between 1.84 and 1.80, adding new crust to the southwestern Fennoscandian Shield (Lahtinen et al. 2005).

3.5 Geological setting of Siilinjärvi carbonatite Complex

The Siilinjärvi carbonatite Complex lies near the city of Kuopio, near the border of Karelia- and Svecofennia Provinces by Raahe-Ladoga Shear Complex (O'Brien et al. 2005; Tichomirowa et al. 2013). It is intruded into granite gneiss rocks covering an area of 14.7 km^2, as a steeply dipping 16 km long lenticular body with width maximum of 1.5 km (Figure 10; Puustinen 1971). The age of the Complex is 2609 ± 6 Ma and is one of the world's oldest carbonatites (O'Brien et al. 2005). It is composed of mainly carbonatite (>50% carbonates), silicocarbonatite (25-50% carbonates), carbonatite-glimmerite (10-25% carbonates) and almost pure glimmerite (0-10% carbonates). Fenites, which have been formed through metasomatic processes have formed a zone surrounding the ore body (O'Brien et al. 2015).

The Siilinjärvi carbonatite Complex is situated in the Archean Iisalmi Complex, a granite gneiss region, nearby its southern border (Figure 10; Puustinen 1971; O'Brien et al. 2005). It is a wedge-shaped region with Karelian quartzites, granites and schists of Savo belt in the east, south and west surrounding the area. To north-east of Siilinjärvi Complex and to north of Nilsiä (Figure 10), lies a Kinahmi quartzite with similar alignment as Siilinjärvi Complex, influenced by the deformation of the surrounding granite gneiss. The Karelian sediments were metamorphosed in the Svecofennian orogeny ca. 1.9 Ga (Puustinen 1971). To the south-west of Siilinjärvi Complex at Siilinjärvi city area, there is also mafic metavolcanite Koivusaari Formation. The Archean basement consists mainly of TTG migmatitic gneisses, ages ranging from Meso- to Neoarchean, and tonalite-quartz diorite granitoids. The migmatitic gneisses have a banded or striped appearance, whereas the granitoids are more homogeneous but typically strongly foliated gneissic granitoids (Lukkarinen 2008).

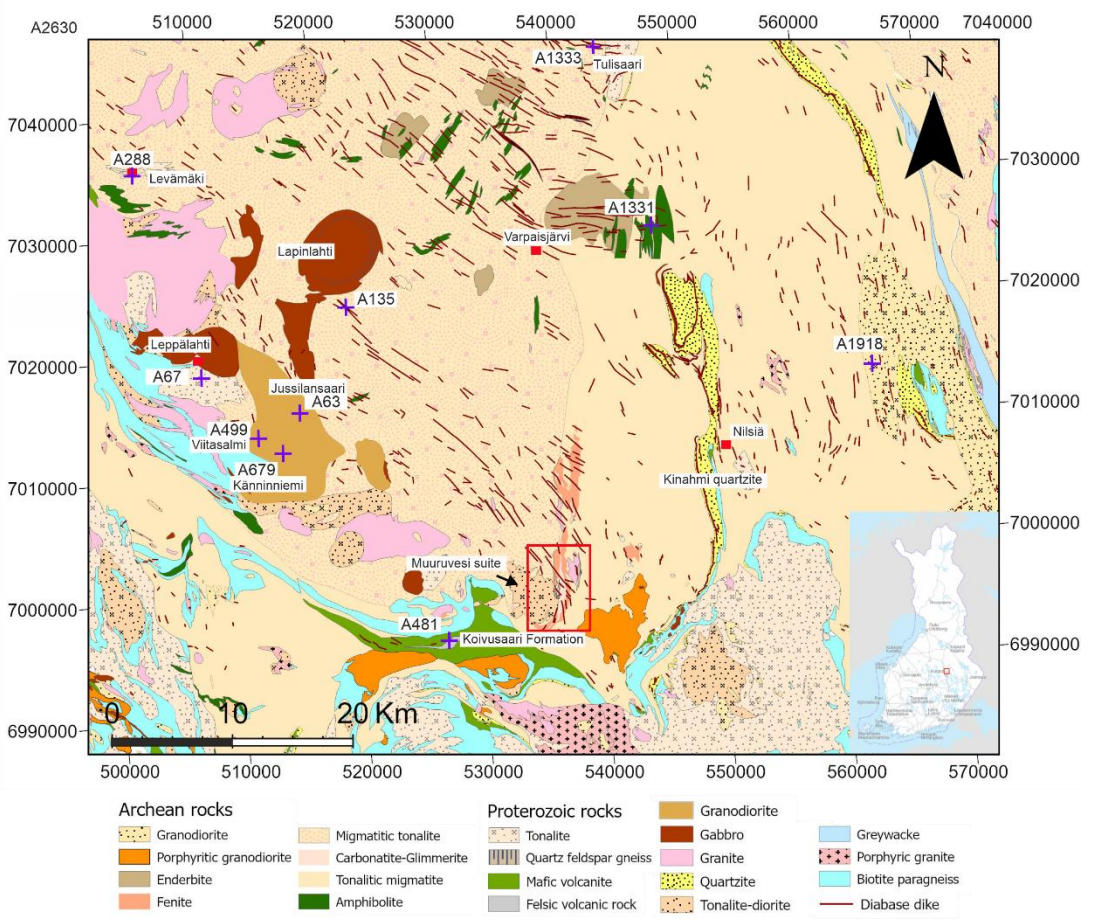

Figure 10. Map of Siilinjärvi and Lapinlahti area. Published age determinations are indicated by purple crosses with corresponding labels. Specific locations mentioned in this study are shown by red boxes and labels. Study area outlined as a red rectangle. Coordinates are given as ETRS-TM35FIN. Modified after bedrock map 1:200 000, produced by GTK. Published age determinations: A1333: Hölttä et al. (2000), A1331: Mänttäri and Hölttä (2002), A1918: Heilimo et al. (2011), A481: Huhma et al. (2018), A679; A63; A499; A67; A288; A135: Paavola (1988).

Although Puustinen (1971) in the first in-depth study initially described much of the surrounding rock as syenite, later studies have reinterpreted these rocks as fenite (O'Brien et al. 2015). Because of this, in this study, I use the term fenite instead of "syenite" when referring to these altered rocks.

The sequence of intrusions began with the emplacement of glimmerite, followed by fenite along its margins and the surrounding rocks (Puustinen 1971). Carbonatite was then intruded among the glimmeritic rocks, creating a series of mixed rocks of carbonatite-glimmerite, with composition varying from almost entirely glimmerite to predominantly carbonatite (Puustinen 1971; O'Brien et al. 2015). Shearing or primary magmatic processes define the boundaries where the country rocks meet the main ore body. To the east of the mine, the main ore-fenite contact is particularly distinct and remarkably retained (O'Brien et al. 2015). The last carbonatitic phase intruded more easily into the

glimmeritic rocks compared to the compact fenite. The transition from carbonatite to a carbonate-rich glimmerite is evident through the penetration of carbonates through fractures within the glimmerite. This process leading to the formation of a relatively uniform carbonate-glimmerite is particularly well illustrated near wide carbonatite lenses (Puustinen 1971). The Complex also exhibits youngest and mostly pure calcite veins (<10 cm thick) which cross-cut the older laminated carbonatite-glimmerite rocks (E. Heilimo, pers. comm., May 22, 2025).

The glimmerite-carbonatite rock series is mainly made up of rocks rich in phlogopite. These rocks vary from almost pure glimmerite, which contains little to no carbonates to carbonate glimmerite and silicocarbonatites. The central ore body is largely dominated by these rocks, with carbonatite making up approximately 1.5% of the main intrusion (O'Brien et al. 2015). The carbonatite is typically light gray, white, or slightly reddish in colour and generally has a medium-grained texture. The primary mineral is calcite, with phlogopite, alkali amphibole, and apatite (Puustinen 1969). It mostly forms thin, vertical veins within glimmerite, especially near the center of the intrusion (Figure 11; O'Brien et al. 2015). The glimmerite is typically medium-grained and varies in colour from reddish-brown to black. Its primary components include phlogopite, alkali amphibole (richterite), and apatite, with zircon and opaque minerals as minor constituents (Puustinen 1969). The amphibole content can make up as much as 50 % of the glimmerite, however it is typically less than 15 % (Puustinen 1971).

Figure 11. Typical glimmerite-carbonatite rock from the main intrusion of the Siilinjärvi mine exhibiting laminated, primary magmatic texture. Modified after O'Brien et al. (2015).

The deposit is characterized by steep, north-south trending shear zones located near its boundaries and within the carbonatite-glimmerite ore. The carbonatite-glimmerite's vertical layering structure has undergone at least two folding events. The initial phase resulted in open to tight folds with nearly horizontal fold axes oriented north and south. The second phase involved strong vertical shearing in a north-south direction, which also affected the ore contacts. This shearing generated small folds, both left- and right-handed, to the more ductile glimmerite. Signs of the later folding are observable in the ore itself and the intersecting Paleoproterozoic diabase dikes (O'Brien et al. 2015).

The fenites formed due to sodium and potassium metasomatism, altering the country rocks. Microcline, amphibole, and pyroxene form the main mineral constituents of the fenites, but various types of fenites also exist, such as those rich in pyroxene or amphibole, those containing carbonates or quartz, and others with aplitic or quartz-aegirine compositions (O'Brien et al. 2015). The Siilinjärvi fenites are characterized by the light green alkali amphibole from the surrounding gneisses (Puustinen 1971). The rise of H_2O-rich fluids and the process of hydrofracturing may have aided the upward movement of the parent magmas through deep crustal shear zones. This movement likely caused fenitization to occur along the path as the fluids interacted with the surrounding rocks (O'Brien et al. 2015).

Appearing in colors such as reddish, greenish-gray, and gray, fenite also shows a range of grain sizes between fine and coarse. The carbonate content is largely a result of later carbonatization (Puustinen 1969). Fenite is present as dikes or irregular bodies within the glimmerite (Figure 12), becoming more frequent closer to the contact with the main marginal fenite. It surrounds the glimmerite-carbonatite complex but small patches of fenite can also be found beyond the main complex (Puustinen 1969; Puustinen 1971). The rock fractures were tightly sealed, which restricted the flow of metasomatic fluids from the carbonatite magma into the surrounding rocks (Puustinen 1971).

Figure 12. Light fenite blocks in the glimmerite from Siilinjärvi mine. Modified after Lukkarinen (2008).

In the southwestern part of the carbonatite Complex is a tonalite-diorite intrusion, part of Muuruvesi suite (Figure 10), which mingles the Complex (O'Brien et al. 2015) and which the 0.5–1.0 m thick, N-S oriented plagioclase porphyry dike cuts across. The Siilinjärvi Complex and the surrounding country rocks are intersected by Paleoproterozoic diabase dikes with basaltic composition. Their width varies from a few centimeters to several meters. These dikes predominantly follow a NW–SE or N-NW–S-SE orientation (O'Brien et al. 2015). It is suggested that more than one generation of mafic dikes have been identified based on contact and relation to other rocks and varying composition, one of which has been linked with the tonalite-diorite intrusion. While most of these dikes exhibit a steep dip, shallow-dipping dikes are also relatively common. Overall, the main minerals of these dikes contain varying proportions of chlorite and biotite, accompanied by feldspar, and more or less amphibole and epidote. Euhedral plagioclase crystals are found, and they are largely altered to sericite and epidote (Mattsson et al. 2019).

4 Materials and methods

The rock samples studied are named EPHE-2015-300.1, EPHE-2015-300.2, EPHE-2015-301.1 and EPHE-2015-303.1, which have been acquired from Siilinjärvi apatite mine in 2015 by Esa Heilimo. The samples have been taken with a rock hammer. The locations of the samples are shown in Figure 13. The dated target rock sample (EPHE-2015-301.1) was interpreted as a hypabyssal dike at the site. The dike is located on the west side of

the Complex, it is parallel to the N-S trending shear zone, and it crosscuts the carbonatite-glimmerite, diabase dikes and Muuruvesi suite tonalite-diorite. This dike has not previously been described. The granodioritic samples EPHE-2015-303.1, EPHE-2015-300.2 and EPHE-2015-300.1 represent Muuruvesi suite tonalite-diorite rocks which is compared to the so-called “microtonalites” of the area.

Two groups of reference data were used to compare the geochemical composition of the rocks studied. The first group consists of quartz-diorites and tonalites and the second of granodiorites, all from undefined suites, analyzed by Paavola (1988), from Lapinlahti and Leppälahti areas (Figure 10). The quartz-diorites and tonalites he describes as medium-grained, homogeneous and mostly foliated. The main minerals include plagioclase, quartz and biotite, with some hornblende, K-feldspar and epidote. The granodiorites he describes as mostly oriented but also many places with uniform appearance. The granodiorites are usually migmatized in the contacts to Archean basement rocks. He describes them as even-grained, grayish-red in colour and relatively homogeneous, with porphyritic feldspars also visible in few places. The main minerals include quartz, plagioclase, microcline, biotite and some accessory minerals such as epidote, titanite and chlorite.

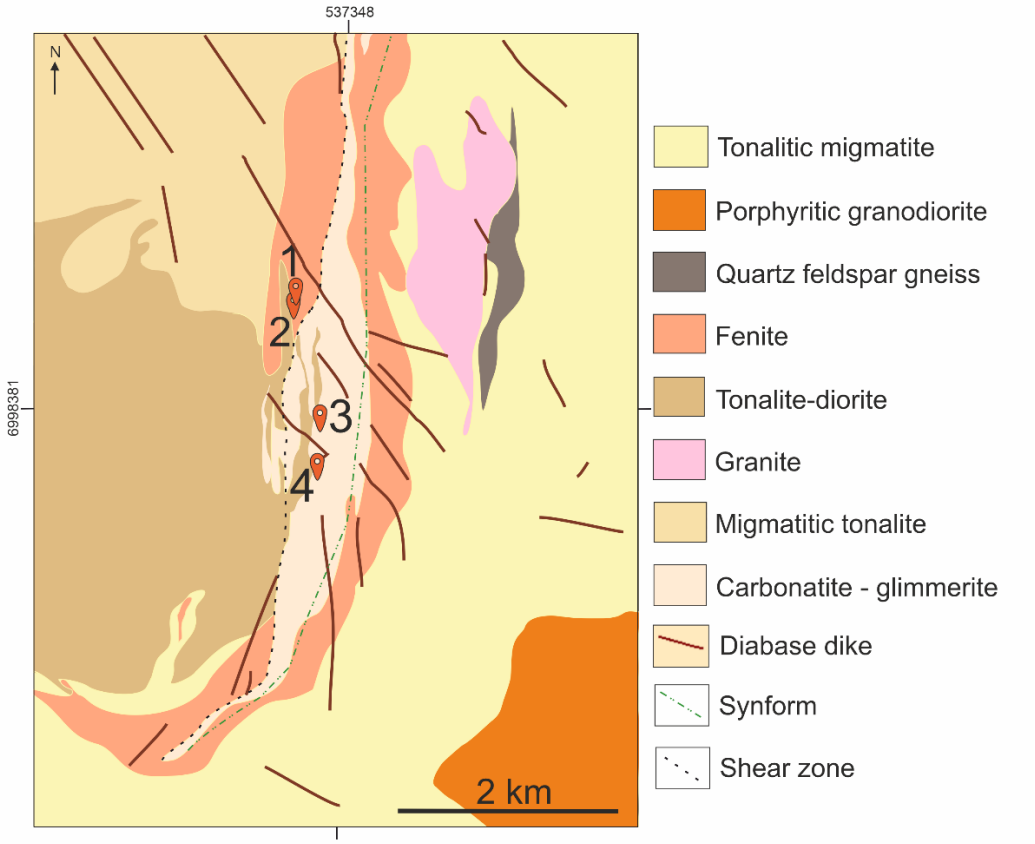

Figure 13. Locations of the studied rock samples and geological map of Siilinjärvi mine area. Locations of rock samples: 1) EPHE-2015-300.2, 2) EPHE-2015-301.1, 3) EPHE-2015-300.1, 4) EPHE-2015-303.1. Coordinates are given in ETRS-TM35FIN. Modified after bedrock map 1:200 000, produced by GTK.

4.1 Thin sections

From each of the four rock samples a counterpart piece of thin section was sawn for the preparation of thin sections. From these, the thin sections were prepared in Geohouse, University of Turku. The thin sections were studied using optical microscopy under both plane- and cross-polarized light. The petrographic analysis focused on identifying mineralogy, grain size, documenting mineralogical alterations and classifying the rock samples using the QAFP classification diagram which categorizes rocks based on quartz, alkali feldspar and plagioclase content (Le Maitre 2002).

4.2 Whole-rock analysis

Whole-rock geochemical analysis was performed by Labtium Ltd for all the samples. The samples were analyzed with X-ray fluorescence (XRF), Labtium automatic sample preparation method 176X. The samples were crushed using a jaw crusher with Mn-steel jaws and ground with tungsten carbide vessel. Major elements analyzed with XRF from

pressed pellet included Si, Ti, Al, Fe, Mn, Mg, Ca, Na, K, P, that are listed as wt% of oxides, according to normal convention. Trace elements analyzed with XRF included As, Ba, Bi, Ce, Cl, Cr, Cu, Ga, La, Mo, Nb, Ni, Pb, Rb, S, Sb, Sc, Sn, Sr, Th, U, V, Y, Zn, Zr. Certain trace-elements were further analyzed by inductively coupled plasma mass spectrometry (ICP-MS) with Labtium method 308PM. These included Ce, Co, Dy, Er, Eu, Gd, Hf, Ho, La, Lu, Nb, Nd, Pr, Rb, Sm, Ta, Tb, Th, Tm, U, Y, Yb, Sc, V, Zr, which are listed as ppm. In this method, the samples were ground using a carbide steel vessel. The samples were completely dissolved using perchloric acid. The whole-rock geochemical data was analyzed and plotted using Geochemical Data Toolkit (GCDkit; Janoušek et al. 2006).

4.3 U-Pb age determination on zircon

The rock sample EPHE-2015-301.1 was used for zircon single grain age dating. The extraction of zircons from the rock sample was done in the laboratory facilities of University of Turku in Geohouse. The rock sample was crushed using a Fritsh pulverisette jaw crusher. The crushed material was then ground with a Fritsch Pulverisette 9 vibrating cup mill with a chrome-free pan. The rock powder was sieved using 300 μm sieve. A total of 1.5 kg of material was gained, which was then panned to obtain heavier minerals. Magnetic separation was performed using a handheld magnet to remove highly magnetic minerals. Heavy liquid separation was done to the sample with methylene iodide, to remove lighter and collect heavier fraction. Further magnetic separation of the heavy minerals was attempted using Frantz Isodynamic Separator Model L-1, that utilizes an electromagnet. The separation was intended to run three times with 0.5, 1.0 and 1.5 A, however, the machine malfunctioned before the first separation was completed. As a result, the rest of the separation was left unfinished, requiring moving to the next part. Zircons were then handpicked, from the sample that was once electromagnetic separated. A total of 119 presumed zircon grains were picked and put on a tape, to be mounted on epoxy. The epoxy mounts were polished to reveal grain interiors. Back-scattered electron images (BSE) and cathodoluminescence (CL) images were taken at the Departments of Physics and Astronomy with Apreo S Scanning Elecron Microscope (SEM) by Thermo Fisher Scientific. However, only 18 of the selected grains were confirmed to be zircons, requiring additional picking of zircons. BSE and CL imaging were repeated for the newly selected grains, confirming 34 additional zircons.

Suitable points from each zircon were selected, and the U-Pb age determination was done at Espoo at Finnish Geosciences Research Laboratory facilities of Geological Survey of Finland with LA-ICPMS Attom (Laser Ablation Inductively Coupled Plasma Mass Spectrometry). A Nu Plasma AttoM single collector ICPMS connected to a Photon Machine G2 laser ablation system was used for the U-Pb dating. The sample grains were ablated in He gas with gas flows of 0.4 and 0.1 1/min within a HelEx ablation cell (Müller et al. 2009). Prior to the entry into the plasma, the He aerosol was mixed with Ar, with gas flow of 0.961 1/min, which was optimized daily. Conditions for the ablation were the following: diameter of the beam: 25 μm, pulse frequency: 5 Hz and beam energy density: 1.63 J/cm^2. Each single U-Pb measurement included a short pre-ablation, 20 s of He flushing, 20 s of on-mass background measurement that was followed by 40 s of ablation with a stationary beam. A calibration standard GJ-1 (609 ± 1 Ma; Horstwood et al. 2016) and two in-house reference samples A 382 (1877 ± 2 Ma; Huhma et al. 2012) and A 1772 (2712 ± 2 Ma; Huhma et al. 2012) were used and run at the beginning and end of session, and at regular intervals throughout the session. The raw data were processed using the program Glitter 2, which applied corrections for the background, laser induced elemental fractionation, mass discrimination and drift in ion counter gains and reduction to U-Pb isotope ratios by calibration to concordant reference zircons (Van Achterberg et al. 2001).

5 Results

5.1 Hand samples

The hand samples of the studied rocks are all dominantly dark gray in colour with lighter to white mineral phases within (Figure 14). The rock sample EPHE-2015-301.1 (Figure 14A) exhibits a dark or black fine-grained matrix with distinct porphyritic texture composed of larger, up to 4 mm sized, plagioclase phenocrysts. The samples EPHE-2015-300.2 and EPHE-2015-303.1 (Figure 14B and C) show very similar colouring and textural characteristics showing moderately coarse-grained texture and evenly distributed light and dark minerals. The sample EPHE-2015-300.1 (Figure 14D) is distinguished from the rest with fine overall grain size and more general darker colour. Lighter phases are less noticeable, giving it a more uniform appearance. Samples EPHE-2015-301.1 and EPHE-

2015-303.1 exhibit relatively homogeneous mineral orientation, while EPHE-2015-300.2 and EPHE-2015-300.1 display random orientation.

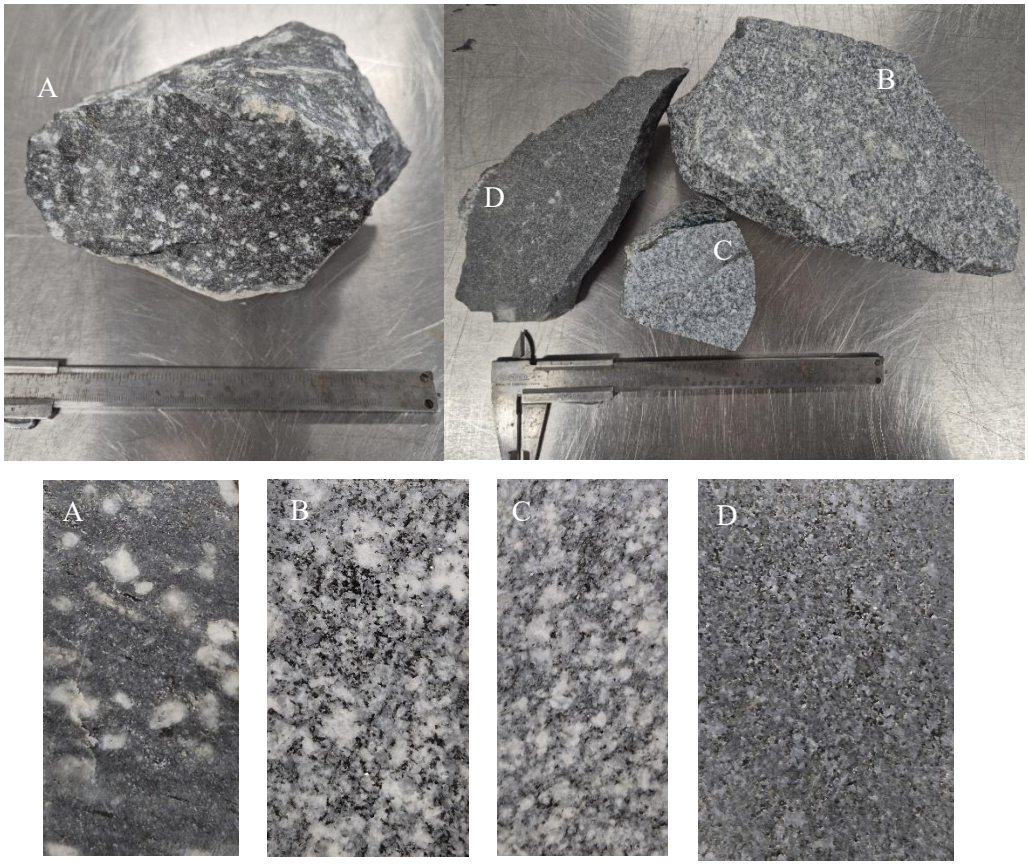

Figure 14. Close up images of the studied rocks in hand samples. A = EPHE-2015-301.1 (plagioclase porphyry), B = EPHE-2015-300.2 (granodiorite), C = EPHE-2015-303.1 (granodiorite), D = EPHE-2015-300.1 (melatonalite). Width of samples in the lower images are approximately 2 cm.

5.2 Petrography

The hypabyssal rock sample EPHE-2015-301.1, selected for age determination, has been identified as a plagioclase porphyry. However, microscopic examination reveals that the phenocrysts include not only plagioclase, but also microcline (Figure 15), exhibiting cross-hatched twinning, both of which are larger than the surrounding matrix. The matrix is finest amongst all the samples, grain sizes approximately 0.05–0.50 mm. The phenocrysts are generally anhedral, with sizes ranging from 0.5 mm to 4.0 mm in diameter. The plagioclase composition is approximately oligoclase, indicating a low anorthite content.

The matrix is evenly textured, composed of quartz, biotite, K-feldspar, epidote, calcite, chlorite, and a few opaque minerals (Figure 15). Quartz in the matrix appears recrystallized based on 120-degree grain boundaries and opaques, checked with reflected light microscope is distinguished as pyrite. Alteration is visible in the phenocrysts, particularly in the plagioclase, which has undergone saussurite and sericite alteration, and has formed secondary clay minerals and epidote group minerals as epidote and clinozoisite. Calcite is also present in the vicinity of the plagioclases. The mafic minerals in the thin section appear oriented.

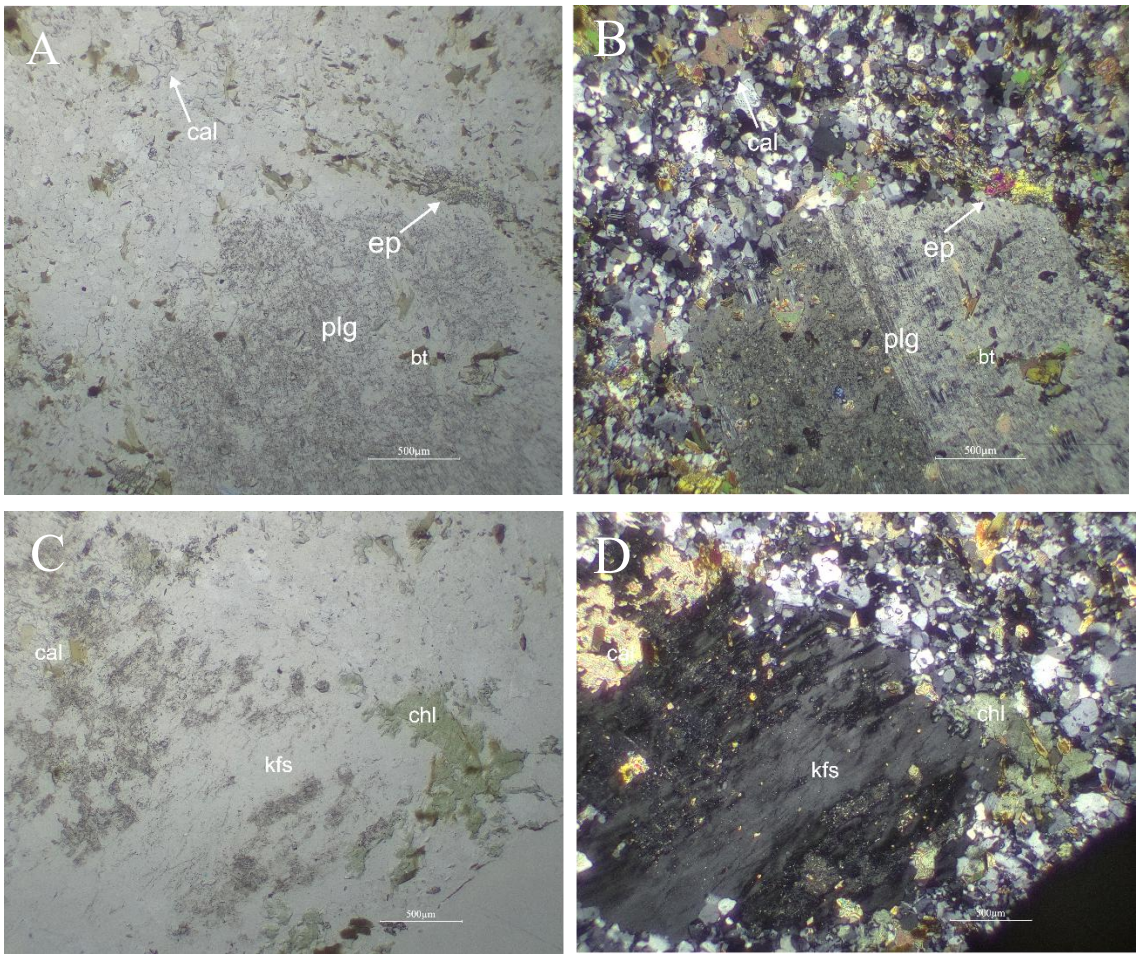

Figure 15. Plane polarized (A and C) and cross polarized (B and D) images of the plagioclase porphyry (EPHE-2015-301.1). Plagioclase porphyries (plg) and alteration to sericite, saussurite and epidote (ep) minerals (A and B). Biotite (bt) alteration to chlorite (chl) (A,B,C and D). Calcite (cal) is found in and near plagioclases and K-feldspars (A,B,C and D).

Sample EPHE-2015-300.1 is identified as a melatonalite. The rock has quite an even grained texture and is mostly randomly oriented (Figure 16A). The modal amount of mafic minerals is significant, highest of all the samples, leading to the prefix mela. The main minerals are plagioclase, hornblende, biotite and quartz, with grain sizes of minerals

other than plagioclase averaging around 0.5 mm. The grains of these minerals exhibit a granular texture, with the plagioclase grains mostly subhedral to anhedral with sizes ranging from 0.3 mm up to 3.0 mm in diameter. The plagioclase exhibits sericitization, saussurization and alteration to clinozoisite and epidote, often forming ring-like structures (Figures 16B and C). Many plagioclase grains also contain inclusions of hornblende and biotite. The sample also includes some opaque minerals that were examined using a reflected light microscope and were identified as pyrite.

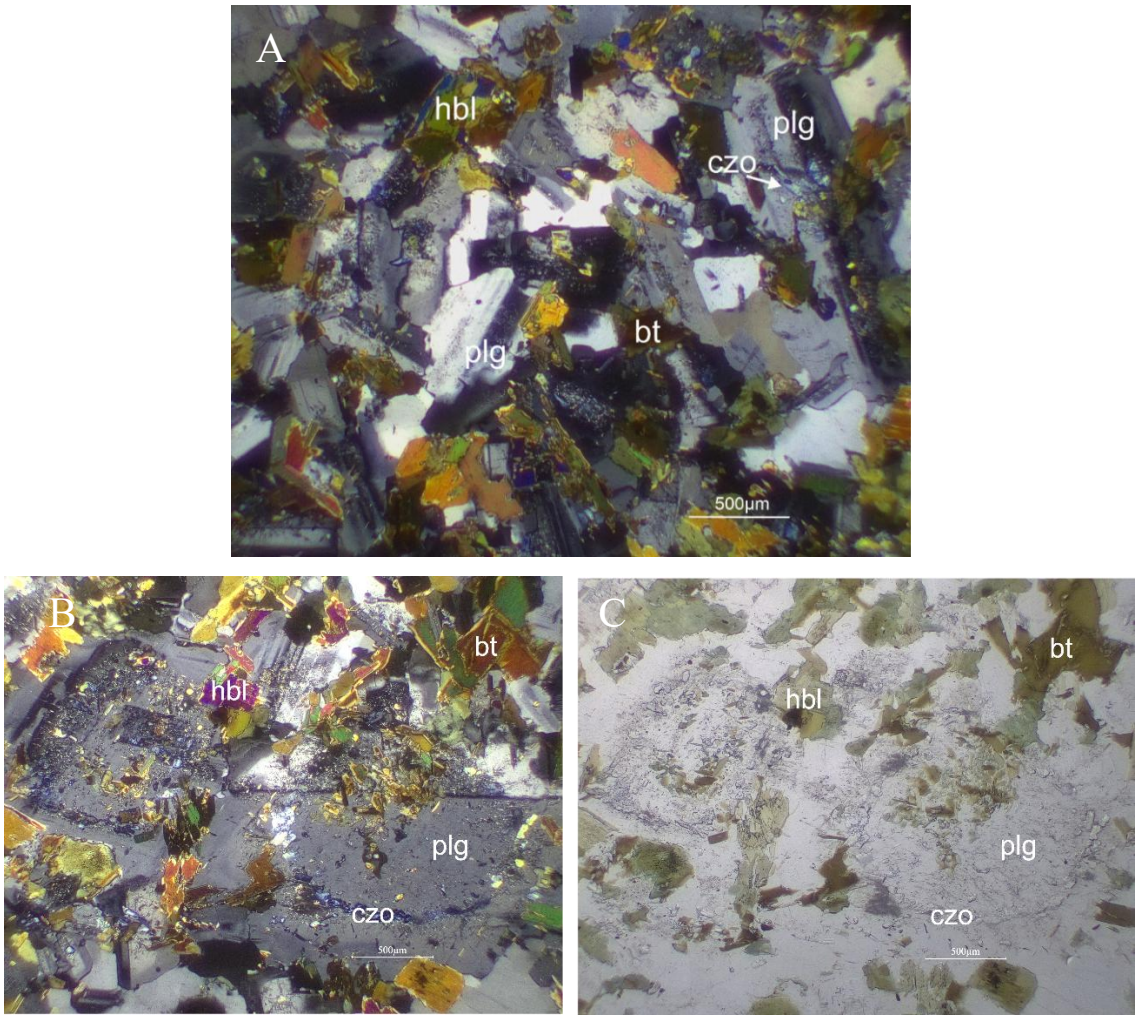

Figure 16. Cross polarized (A and B) and plane polarized (C) images from the melatonalite (EPHE-2015-300.1). Image A, showing the more typical texture for the rock. Subhedral plagioclases (plg) and considerable amount of hornblende (hbl) and biotite (bt). Plagioclase alteration to epidote group minerals, such as clinozoisite (czo).

Sample EPHE-2015-303.1 is identified as a grandiorite based on the QAPF classification. The rock contains a major amount of quartz, along with plagioclase, K-feldspar, biotite, and chlorite (Figure 17). The matrix exhibits principally an even grained, granular texture,

although plagioclase grains can be larger than the rest, up to 3.0 mm in diameter, and often appear sub- to anhedral. The average grain size of matrix minerals is around 0.5 mm. Some K-feldspar grains exhibit perthite intergrowths. Plagioclase shows alteration, with transformation to clinozoisite, epidote, sericite and saussurite. Allanite is also present, though in smaller amounts, with a grain size approximately 0.4 mm in diameter. The biotite has altered to chlorite and the quartz shows signs of recrystallization, as the grain boundaries meet at approximately 120-degree angles.

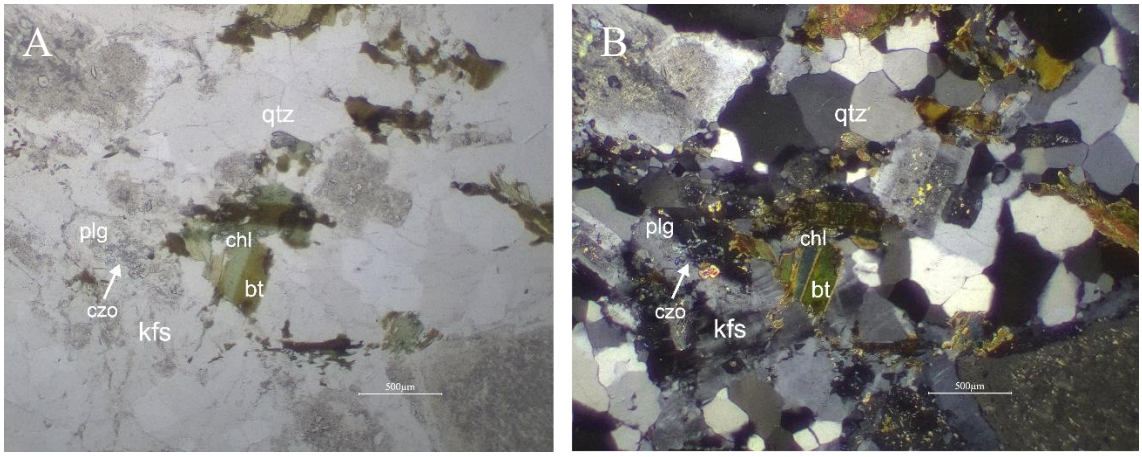

Figure 17. Plane polarized (A) and cross polarized (B) images of the granodiorite (EPHE-2015-303.1). Subhedral plagioclases (plg) with saussuritization and sericitization, and alteration to epidote group minerals, such as clinozoisite (czo). Also grains of K-feldspar (kfs), recrystallization of quartz (qtz) and biotite (bt) alteration to chlorite (chl).

Sample EPHE-2015-300.2 is identified as a granodiorite based on the modal amount of minerals. The rock is generally medium- to coarse-grained and exhibits mortar texture, with some areas containing larger subhedral plagioclase crystals, up to 3.0 mm large grains in diameter, that stand out from the matrix. The mineral composition consists primarily of plagioclase, quartz and biotite, although quartz is present in lesser amounts than in previous EPHE-2015-303.1 granodiorite. However, biotite is present in slightly larger amounts than in the previous granodiorite. The sample rock also contains chlorite, epidote and clinozoisite that are mainly found as alteration products within the plagioclase. The grain size of the matrix varies around 0.5 mm in diameter. The plagioclases have also altered to saussurite and some sericite. There is a minor presence of K-feldspar and few opaque minerals. Additionally, some allanite can be found from the thin section (Figure 18).

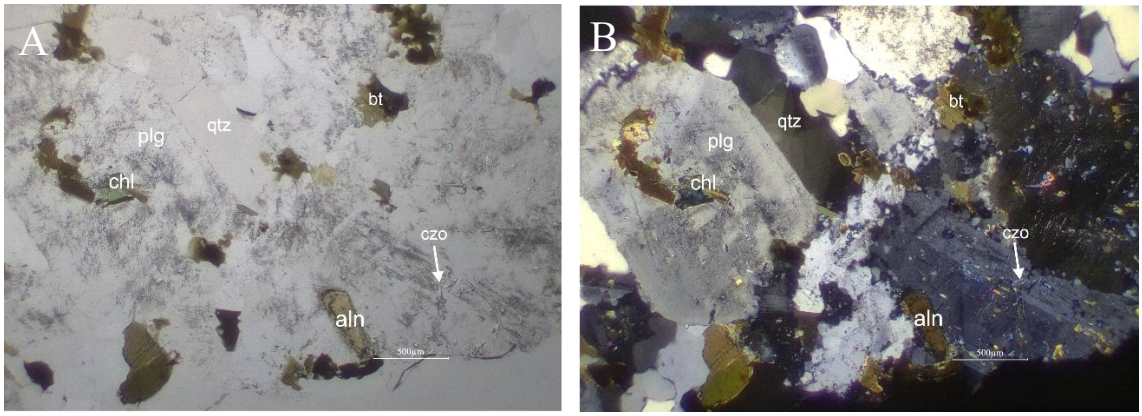

Figure 18. Plane polarized (A) and cross polarized (C) images of the granodiorite (EPHE-2015-300.2). Plagioclase (plg) altered to saussurite and epidote-group minerals such as clinozoisite (czo) and also allanite (aln) is found. Rock contains quartz (qtz) and biotite (bt) altering to chlorite (chl).

5.3 Whole-rock geochemistry

The four rock samples studied exhibit difference in SiO_2 content, varying between 56.17 and 71.84 wt% (Figure 19). The plagioclase porphyry sample (EPHE-2015-301.1) has a slightly higher alkali content than the rest of the samples. In the diagram alkali Na_2O + K_2O vs silica SiO_2 (TAS) by Middlemost (1994), the previously determined melatonalite sample based on observed mineralogy, plotted to the diorite field. The previously determined granodiorite (EPHE-2015-300.2) plotted to the granodiorite field. The sample EPHE-2015-303.1 plotted to the granite field, which is slightly different than was previously determined. The sample EPHE-2015-301.1, characterized as plagioclase porphyry, plotted to the quartz monzonite field. This would also be consistent with QAFP classification as its quartz content is low and existed only as minor mineral in the matrix, and the plagioclase and K-feldspar content were high and almost equal, as indicated in the amount of $Na_2O + K_2O$. The sample rocks, except for the plagioclase porphyry, follow the reference group rocks very well, as the reference quartz-diorites and tonalites mostly fall into the diorite and granodiorite fields, and the reference granodiorite group also plots mainly to the granite field indicating similar compositions with the sample rocks. Even though the reference granodiorites also partially plot to the quartz monzonite field, the plagioclase porphyry has even higher alkali content than the reference group.

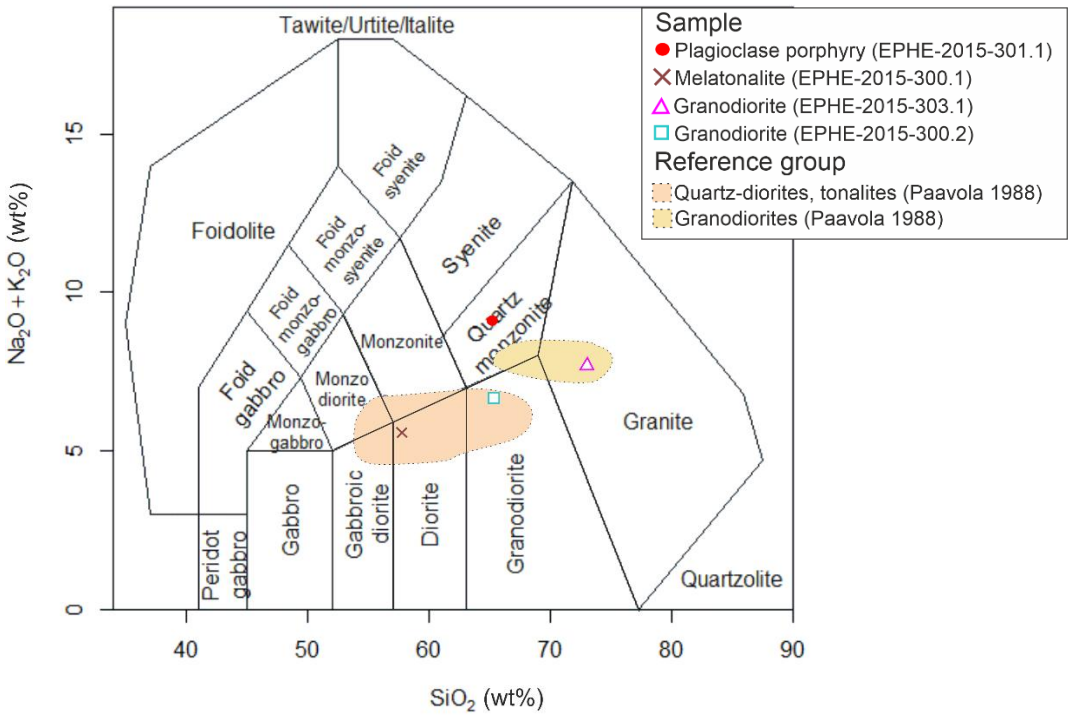

Figure 19. Studied sample rocks plotted with reference groups in total alkali versus SiO_2 (wt%) diagram by Middlemost (1994).

In Figure 20A all the studied rock samples plot into the magnesian field in the $FeO_{tot}/(FeO_{tot}+MgO)$ versus SiO_2 diagram by Frost et al. (2001), which distinguishes ferroan and magnesian granitoids. The reference groups also plot mainly into the magnesian field. In Figure 20B, all the samples except the plagioclase porphyry plot to the calc-alkalic field, while it plots to the alkali-calcic field. The reference granodiorite group (Paavola 1988) plots in similar manner as the granodiorite and melatonalite, and it also exhibits similar trend as the more felsic granodiorite and plagioclase porphyry. In Figure 20C the rock samples are plotted in A/CNK - A/NK diagram by Shand (1943) which classifies the rocks based on their alumina and alkali content. All the samples fall within the metaluminous field. The plagioclase porphyry and the more felsic granodiorite exhibit slightly lower A/NK ratio compared to the melatonalite and the other granodiorite, placing them closer to a value of 1, indicating more balanced alumina and alkali composition. The reference group rocks however varies more than the sample rocks, and in addition to the metaluminous field they plot to the peraluminous field.

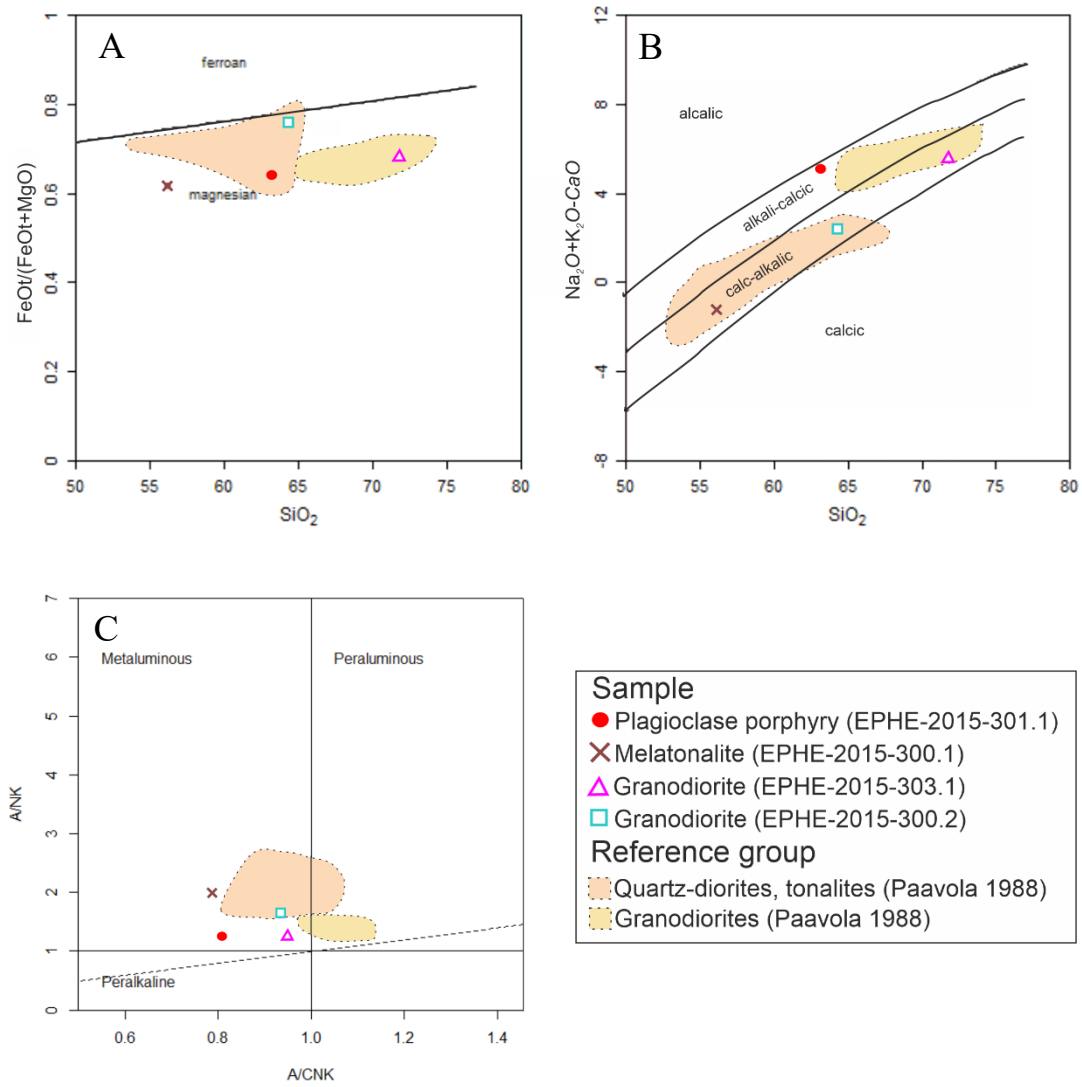

Figure 20. Granite tectonic discrimination binary diagrams of studied sample rocks and reference group rocks. A) $FeO_{tot}/(FeO_{tot}+MgO)$ versus SiO_2 diagram (wt%) (Frost et al. 2001). B) Na_2O+K_2O-CaO versus SiO_2 diagram (Frost et al. 2001). C) A/CNK ($Al_2O_3/(CaO+Na_2O+K_2O)$ versus A/NK ($Al_2O_3/(Na_2O+K_2O)$ (mol. %) diagram (Shand 1943).

Figure 21 shows binary diagrams of major oxides versus SiO_2 content. Corresponding numerical data can be found in Appendix 2. The granodiorite (EPHE-2015-303.1) with the highest SiO_2 content, exhibit relatively higher values in only K_2O and Na_2O contents and relatively low values in all the other oxides (Al_2O_3, CaO, Fe_2O_3, MgO). The Al_2O_3 value is however notably lower than in the other rocks. The melatonalite (EPHE-2015-300.1), however, with the lowest SiO_2 content, exhibits the opposite trend with the highest values of Fe_2O_3, MgO, CaO and also high values of Al_2O_3, but the lowest values with K_2O and Na_2O. The sample plagioclase porphyry (EPHE-2015-301.1), have the highest values of K_2O and Na_2O, and similarly low values of Fe_2O_3 and MgO like the sample

EPHE-2015-303.1. The CaO content falls in between the highest and lowest values, and the Al_2O_3 content is also in the higher value end. The other granodiorite (EPHE-2015-300.2) has similarly low value in K_2O as the melatonalite, but similar concentrations in Na_2O as the plagioclase porphyry and the other granodiorite. The amount of Al_2O_3 is the highest in this sample, but CaO is similar as in the plagioclase porphyry. It also has an intermediate amount of Fe_2O_3, more than the plagioclase porphyry but the MgO content is lower. The samples correlate well with the reference group rocks. The plagioclase porphyry and the granodiorite with more SiO_2 follow the reference granodiorites the best. The melatonalite and granodiorite samples with more mafic content, plot mainly according to the reference group (Paavola 1988) quartz-diorites and tonalites.

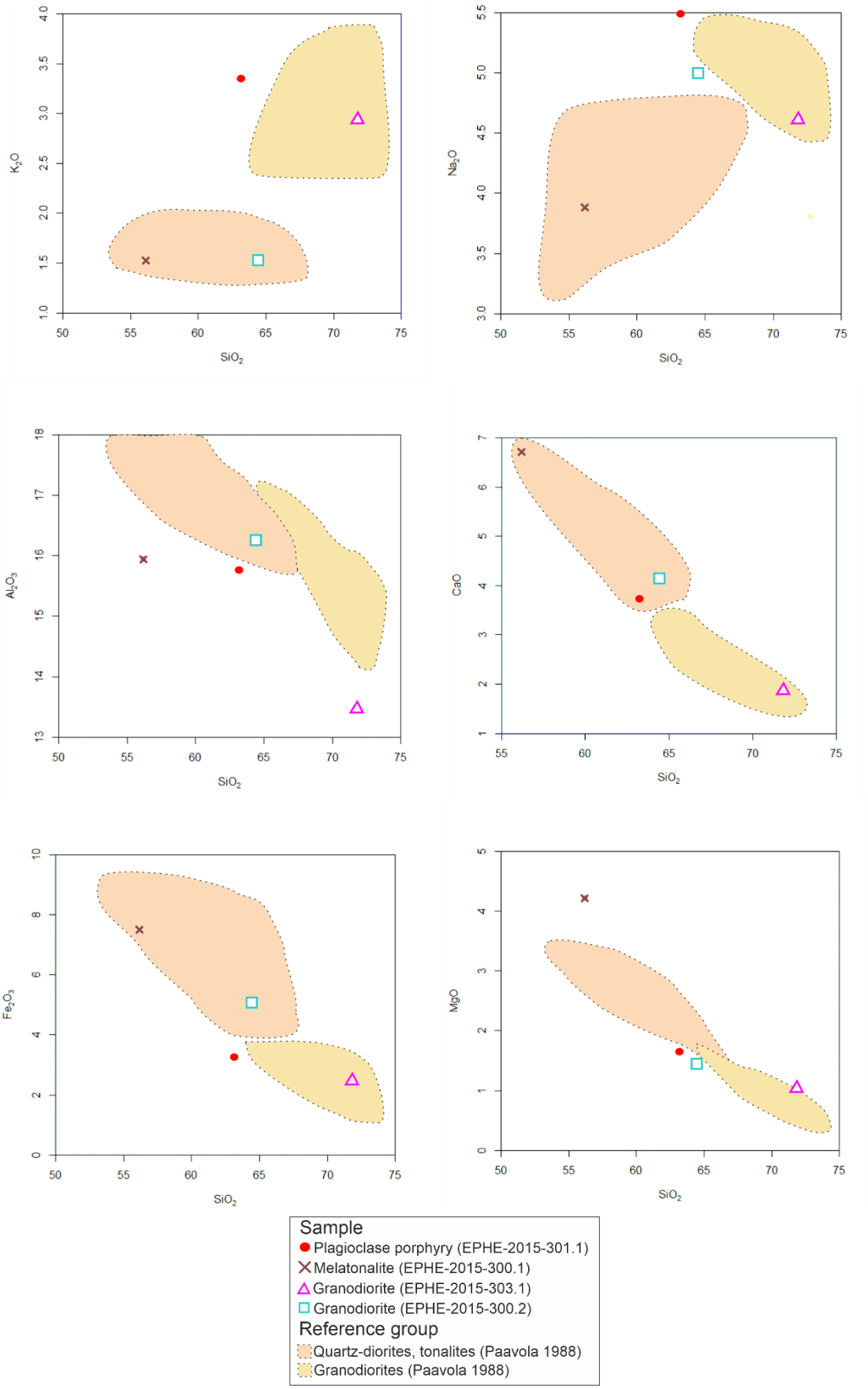

Figure 21. Studied samples and reference groups plotted in binary diagrams of major elements (wt%) versus SiO_2 (wt%).

All the samples exhibit similar downward trends in the chondrite normalized (Boynton 1984) REE- diagram (Figure 22). The plagioclase porphyry contains lowest values, while the granodiorite exhibits highest values. The granodiorite (EPHE-2015-300.2) shows significant LREE enrichment compared to others, but similar concentrations in HREE with the other rocks. While the melatonalite exhibits lower LREE values than the more felsic granodiorite (EPHE-2015-303.1), it is relatively enriched in HREE in comparison to it, showing similar values with the granodiorite. The granodiorites exhibit deepest slopes and the plagioclase porphyry and melatonalite have similar more gentle slopes. There is also no clear Eu anomaly in any of the studied samples.

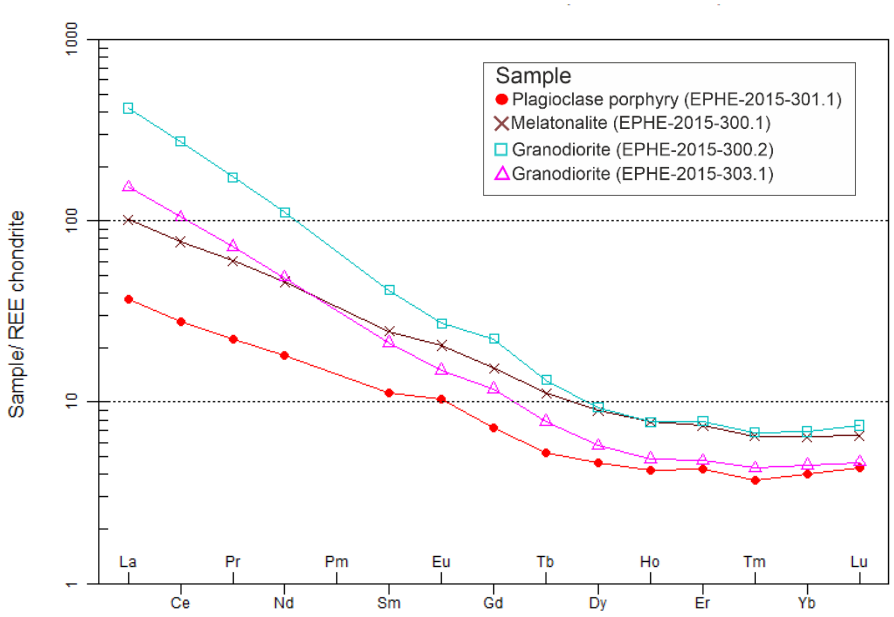

Figure 22. Studied samples in chondrite normalized REE-spider plot (Boynton 1984).

In Figure 23 the studied sample rocks are plotted in Primitive Mantle-normalized (Sun and McDonough 1989) spider plot. The samples studied exhibit similar, mostly enriched, trends in the concentration of elements. Additionally, they display a similar trend as in the chondrite normalized diagram (Figure 22), where the plagioclase porphyry has mostly the lowest values and the more mafic granodiorite has mostly the highest values. Anomalies of Nb, P and Ti are visible, however none of the samples are depleted in any of the elements in comparison to primitive mantle. All the samples are highly enriched in Ba and Pb in comparison to the primitive mantle, the plagioclase porphyry having the

highest Pb values. However, the amount of Pb in the melatonalite was below the detection limit of ca. 0.003 wt%, which has then been represented as half of the detection limit value. There is also a major difference with La and Ce values between samples, where the plagioclase porphyry is relatively depleted in these elements in comparison to the more mafic granodiorite, which is highly enriched in these elements, but similar trends can also be observed from the values of Th, Pr, Nd and Zr.

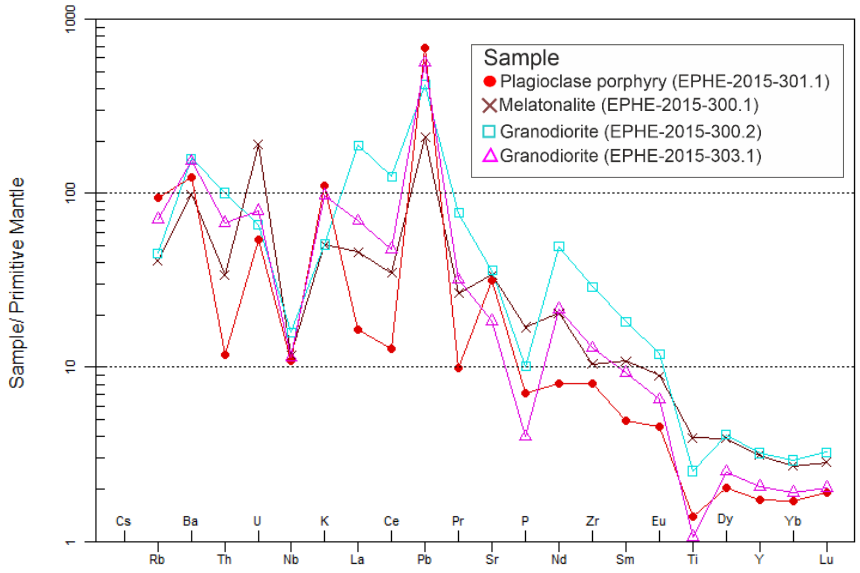

Figure 23. Studied samples in Primitive Mantle-normalized multi-element diagram (Sun & McDonough 1989).

5.4 Zircon U-Pb results

A total of 52 zircons from the plagioclase porphyry (EPHE-2015-301.1) were picked for in situ zircon analysis. By examining the BSE and CL images, four of the zircon grains were discarded due to poor internal structure and potential lead loss. The colour of all zircon grains picked appeared weakly transparent pink under magnification. The lengths of the zircons varied between 0.09 and 0.25 mm. Few of them were only broken parts of zircons, so even larger zircons could possibly be found. Few zircons exhibit prismatic to subrounded shapes, but mostly stubby and equant or sub- to anhedral shapes (Corfu et al. 2003). Growth zoning is visible in some grains, but mostly complex zoning patterns are visible (Figures 24 and 26 grains 1;10, 1;5, 2;21, 2;14). Thickness of sections with growth zoning varies between 0.01 and 0.15 mm.

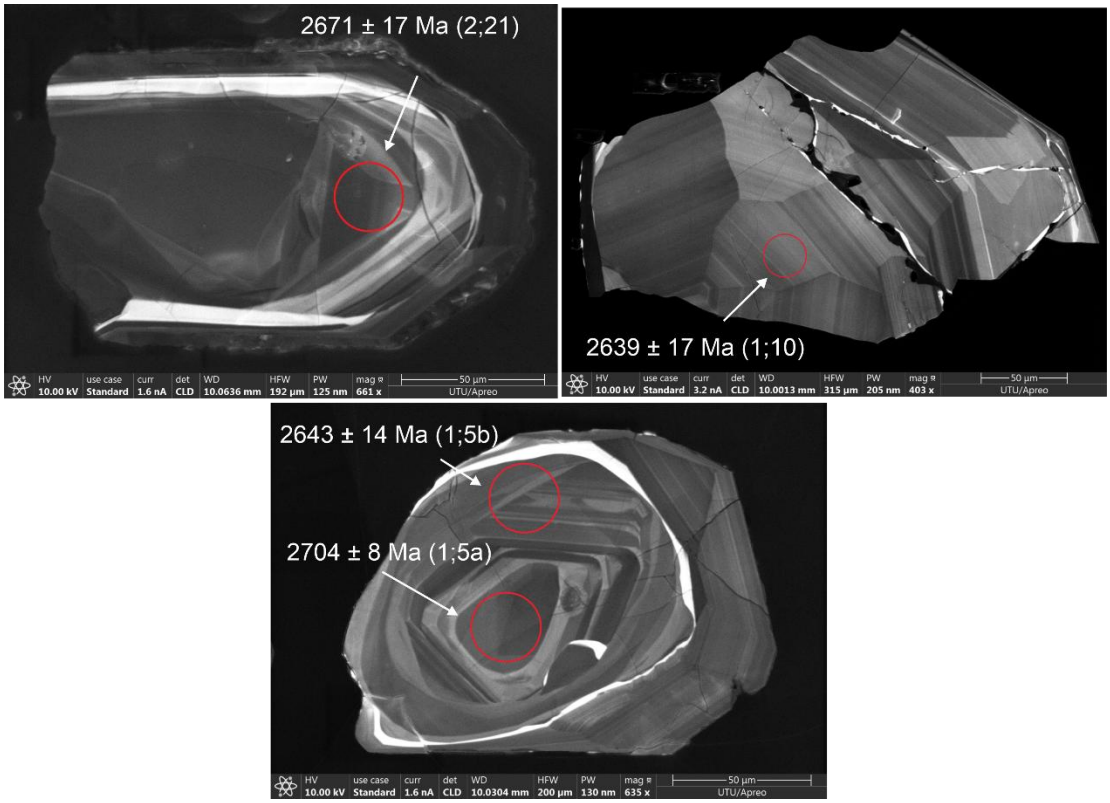

Figure 24. CL images with representative complex zoning patterns from sample EPHE-2015-301.1. The ages presented are $^{207}Pb/^{206}Pb$ ages with 1σ errors. Mount and grain/spot number in parenthesis.

Many of the zircon grains have xenocrystic cores, sizes varying between 0.03 and 0.08 mm. The cores have irregular surfaces, with internal zoning that is abruptly cut off, and can separate the cores from rims with growth zoning (Figure 26, grains 1;1, 2;14, 2;33; Corfu et al. 2003). In zircon grain 1:1 (Figure 26), two core generations are visible. Metamictization is also visible in many grains, as high-U core, dark in CL images, cause expansion and fracturing in on the rims (Figure 25, grains 1;3, 2;1, 2;17). In BSE images it is especially noticeable, as the core is intact and has caused fracturing in the surrounding rim, creating a clear contrast between the core and the damaged outer zones. The width of the fractures varies between 0.01 and 0.05 mm. A few grains also contain small (between 0.003 and 0.025 mm) inclusions which appear black in BSE images (Figures 25 and 26, grains 1;3 2;1 and 1;7), and a lot of grains are heavily fractured.

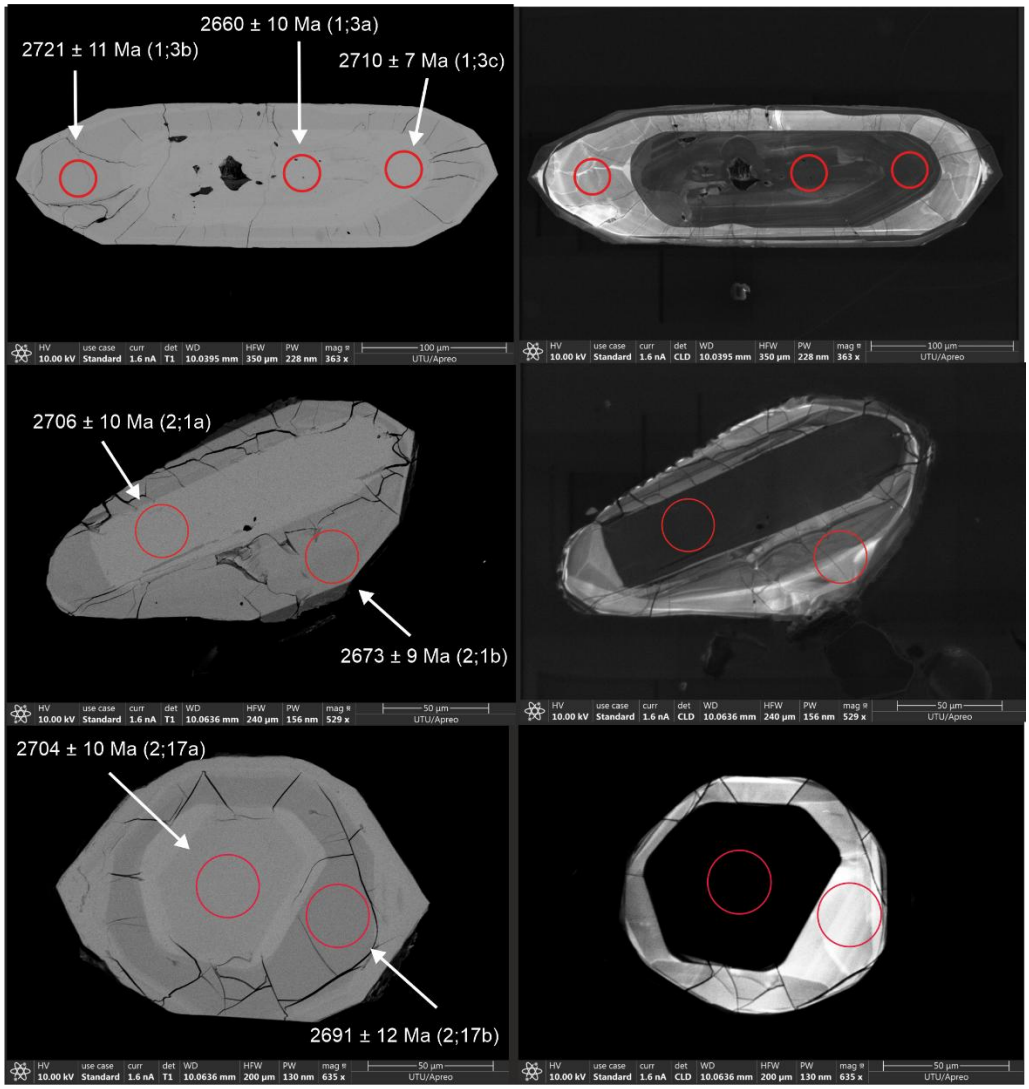

Figure 25. BSE (left) and CL (right) images of metamictization induced fracturing from sample EPHE-2015-301.1. The ages presented are $^{207}Pb/^{206}Pb$ ages with 1σ errors. Mount and grain/spot number in parenthesis.

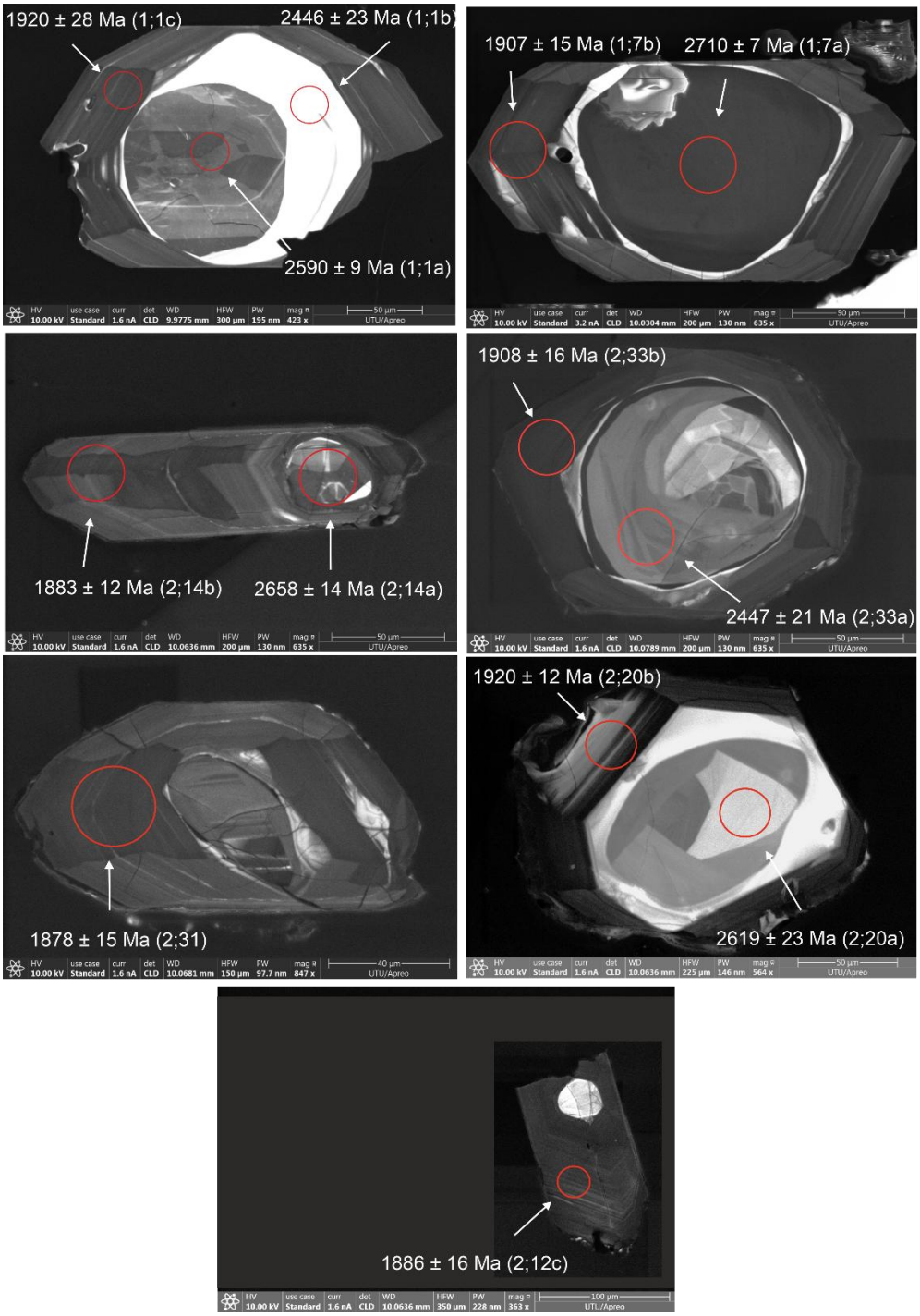

Figure 26. CL images showing xenocrystic cores and seven youngest zircon ages from sample EPHE-2015-301.1. The ages presented are $^{207}Pb/^{206}Pb$ ages with 1σ errors. Mount and grain/spot number in parenthesis.

Of the 49 selected zircons for the age determination, 83 in situ analyses were performed with a spot size of 25 µm. U-Pb age determination data can be found from Appendix 3. The age range of all analysis spots is very broad and youngest and oldest measured $^{207}Pb/^{206}Pb$ ages are 1883 ± 12 Ma and 2991 ± 20 Ma, respectively. Most of the ages fall between 2500 and 2800 Ma (Figure 27B). Five different populations have been identified

based on age distribution and concordance (Figure 27A). All analysis spots in the orange, green and grey populations are taken from the core of zircons, or near the core but not from the outermost rims. All discordant analysis spots plotted above the concordia curve.

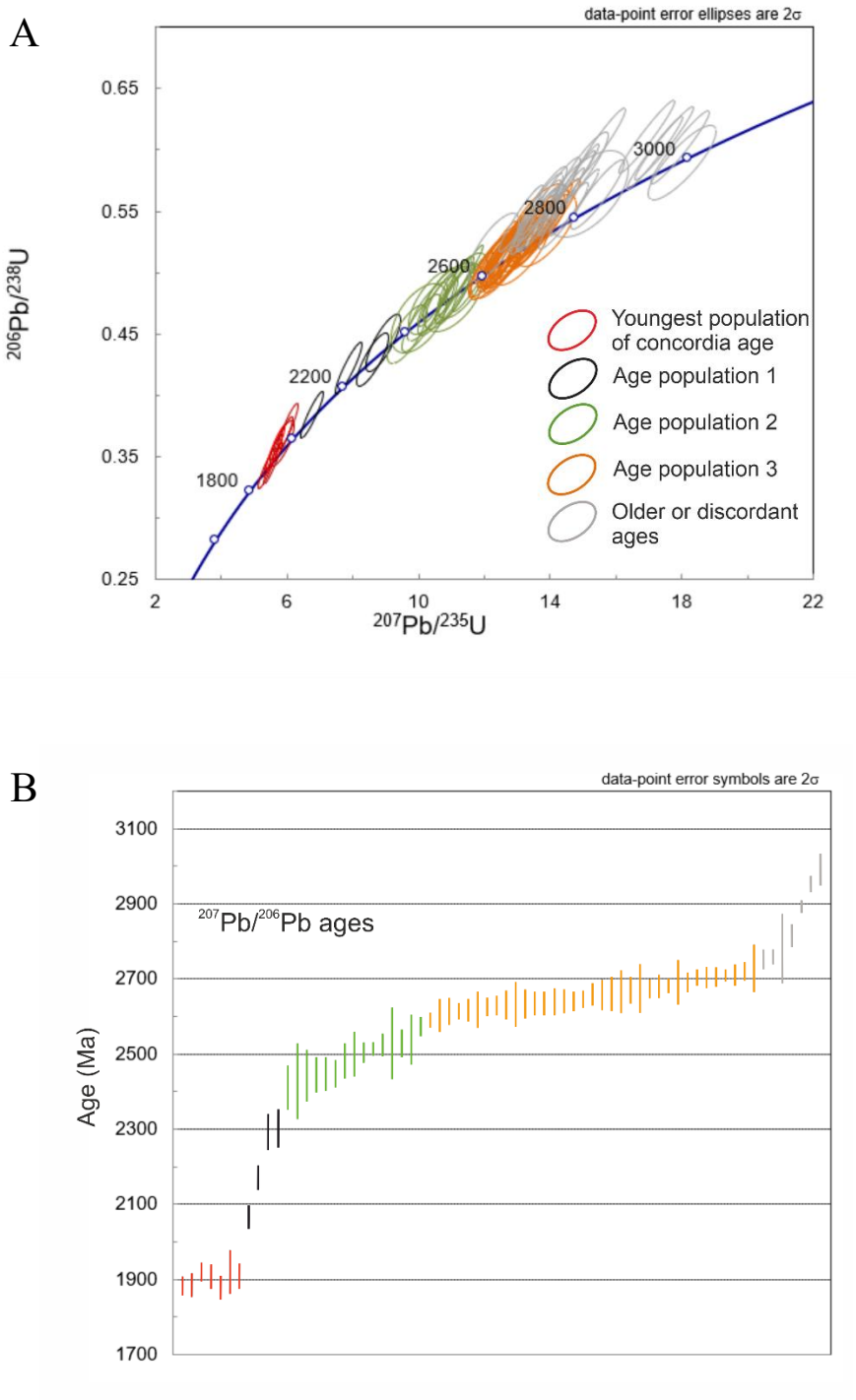

Figure 27. A) All concordia zircon ages from the sample EPHE-2015-301.1. B) $^{207}Pb/^{206}Pb$ age results with their errors of analyses with >95% of concordance.

From the youngest ages, three concordant ones were taken that gave concordia age of 1900 ± 14 Ma (Figure 28). These include analysis points 2;14b, 2;12c and 2;20b (Figure 26), with individual $^{207}Pb/^{206}Pb$ ages 1883 ± 12 Ma, 1886 ± 16 Ma and 1920 ± 12 Ma, respectively. They have xenocryst cores and the analysis to yield young ages were taken from the outermost rims of the grains, exhibiting growth zoning. Four more analysis spots, 1;1c, 1;7b, 2;31 and 2;33b, (Figure 26) gave as young $^{207}Pb/^{206}Pb$ ages (1920 ± 28 Ma, 1907 ± 15 Ma, 1878 ± 15 Ma and 1908 ± 16 Ma, respectively), however they were discordant. Despite that, the locations of the spots are situated in similar setting as the concordant ones.

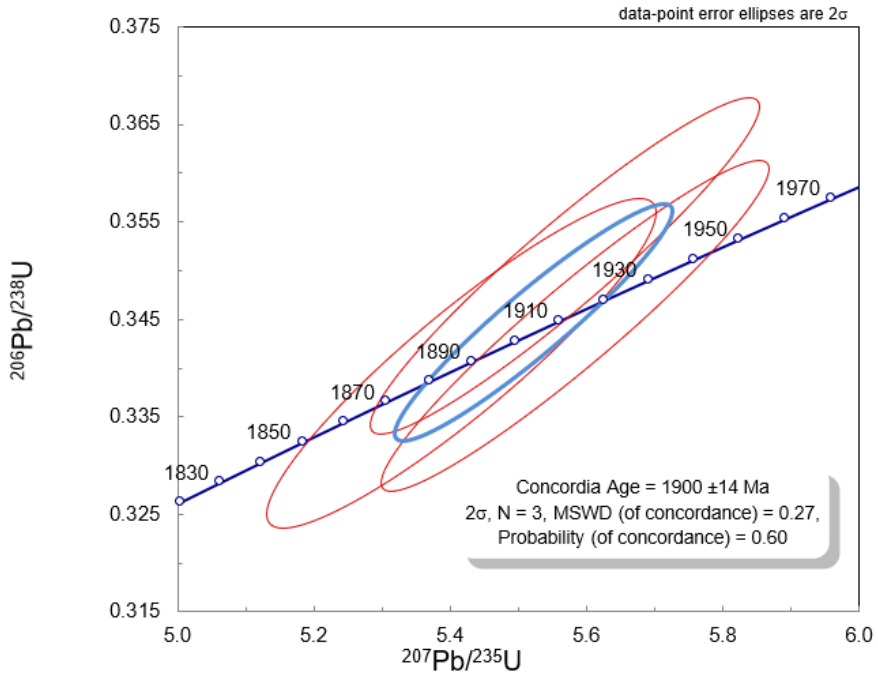

Figure 28. Zircon U-Pb concordia diagram for sample EPHE-2015-301.1. Data from three analyses define a concordia age of 1900 ± 14 Ma.

A weighted average age (Figure 29) was calculated for the concordant analysis points, as well as the four slightly discordant spots (Figure 26, 1;1c, 1;7b, 2;31 and 2;33b), as they exhibited similar characteristics, taken from the outermost rim with growth zoning. The weighted average age for these is 1899 ± 17 Ma with MSWD 1.5 and probability of 0.18. Including the slightly discordant spots can be justified by their location in the zircon rims and the similarity to the concordant spots.

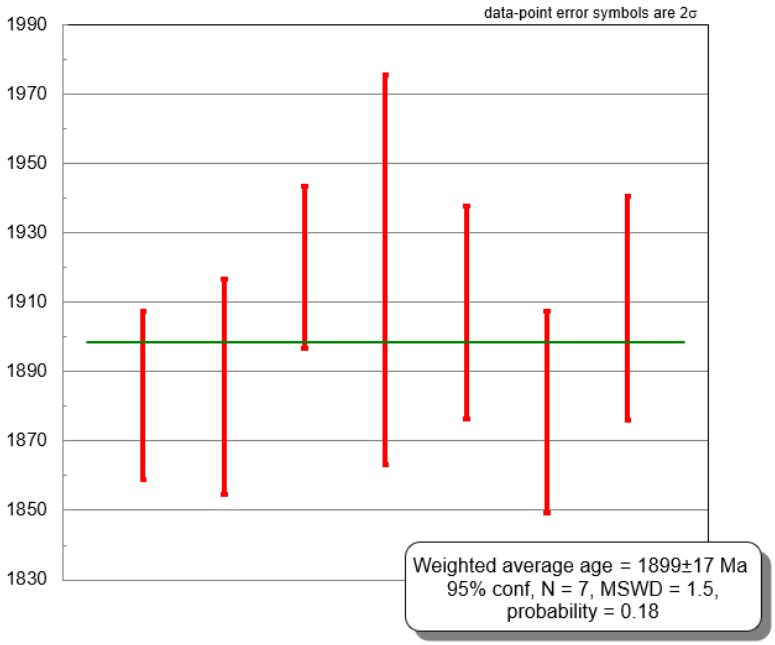

Figure 29. Weighted average age plot of seven $^{207}Pb/^{206}Pb$ zircon ages representing the youngest population from sample EPHE-2015-301.1.

The U-Pb zircon geochronology has yielded a concordia age of 1900 ± 14 Ma for the plagioclase porphyry dike with a complex array of older inherited zircon ages. The following discussion will analyze the implications of these findings, focusing on two primary scenarios for interpreting the ~1.9 Ga age: as either a primary Svecofennian crystallization age or a Svecofennian metamorphic overprint.

6 Discussion

6.1 Interpreting zircon age data

This study investigated the age of potentially youngest observed magmatism in the Siilinjärvi mine area. Two possible interpretations of the concordia age from the youngest samples have been identified. The U-Pb zircon dating of the plagioclase porphyry yielded a concordia age of 1900 ± 14 Ma (Figure 28). This could be interpreted as the crystallization age, suggesting that the rock is Svecofennian in age or it may alternatively represent a metamorphic overprint.

The first interpretation considers the concordia age of 1900 ± 14 Ma (Figure 28) as the primary crystallization age of the plagioclase porphyry dike. This view is supported by

the seven zircon analyses that gave the youngest ages (Figure 26), as the spots located on the outermost rims that exhibited magmatic growth zoning, indicating that these rims crystallized during later stages of magma evolution. Majority of the zircon in situ analysis gave older results (Figure 27), because majority of the spots were located somewhere in the middle of the grain or the core (Figure 22). One possible explanation could be that if more analysis spots would have located in the outermost rims, more younger results could have been obtained. However, the sizes of the zircons were too small to fit the beam diameter (25 μm) to the rims, or the outermost rims were too small-scale. All of these seven zircon grains also contained clear xenocrystic cores, and five of the grains had age analysis taken from the core, all of them giving older ages (Figure 26). By analyzing other minerals from the sample, metamorphic age for the rock could have been acquired. The plagioclase porphyry rock has possibly been metamorphosed in the same process that has metamorphosed the other similar age tonalite-diorite rocks from the area.

The alternative interpretation is that the 1900 ± 14 Ma age (Figure 28) reflects a metamorphic event or is an apparent age resulting from a lead loss episode from older zircons. A discordia line was fitted to the U-Pb data (Figure 30) with anchored lower intercept at 1900 Ma, representing Svecofennian age, which yielded an upper intercept age of 2584 ± 27 Ma. This upper intercept is notably close to the age of the Siilinjärvi carbonatite (2609 ± 6 Ma; O'Brien et al. 2005), suggesting that the porphyry could have crystallized during the Archean eon, with the ca. 1900 Ma age likely reflecting a high temperature event.

Further evidence supporting a metamorphic origin for the 1900 Ma age comes from Th/U ratios of the zircons (Appendix 3). In Figure 31 the ratio of Th and U of each zircon analysis is plotted to a diagram with the corresponding $^{207}Pb/^{206}Pb$ age. The zircon spots yielding the youngest ages (1900 ± 14 Ma) have Th/U ratios ranging from 0.026 to 0.072. For the rest of the samples the ratio is a minimum of 0.1. Th/U ratios of zircons have been used to identify magmatic and metamorphic zircons (Kirkland et al. 2015). Magmatic zircons generally exhibit Th/U values >0.5, while metamorphic zircons often have ratios of <0.1 (Kirkland et al. 2015; Yakymchuk et al. 2018). Th/U ratio of zircons could also be correlated with the whole-rock composition, to see whether the zircon grain grew in equilibrium with the same melt as the host rock, or is inherited and would suggest zircon heterogeneity (Kirkland et al. 2015). When adding a line of the Th/U ratio of the whole-

rock, it can be observed that many of the older zircons share more similar ratio with the whole-rock, values varying mostly between 0.3 and 0.9. This suggest that these older zircons may have grown in equilibrium with the current rock or were inherited from a source with comparable Th/U characteristics. According to the fitted discordia and the low Th/U ratios of the youngest zircon rims, which differ significantly from both the older zircons and the approximated whole-rock ratio therefore, could suggest that they formed under different conditions than the rock. However, it is important to note that Th/U ratios are influenced by many factors, including crystallization of other Th-U bearing minerals, such as monazite or titanite, P-T conditions of metamorphism and melt composition (Kirkland et al. 2015; Yakymchuk et al. 2018). Monazite can be a significant reservoir for thorium, and if it crystallizes before or at the same time as metamorphic zircon, it can lead to low Th/U ratios in zircon. However, if the metamorphic zircon developed close to peak temperature conditions and before for example monazite, it may also lead to higher Th/U ratios (Yakymchuk et al. 2018).

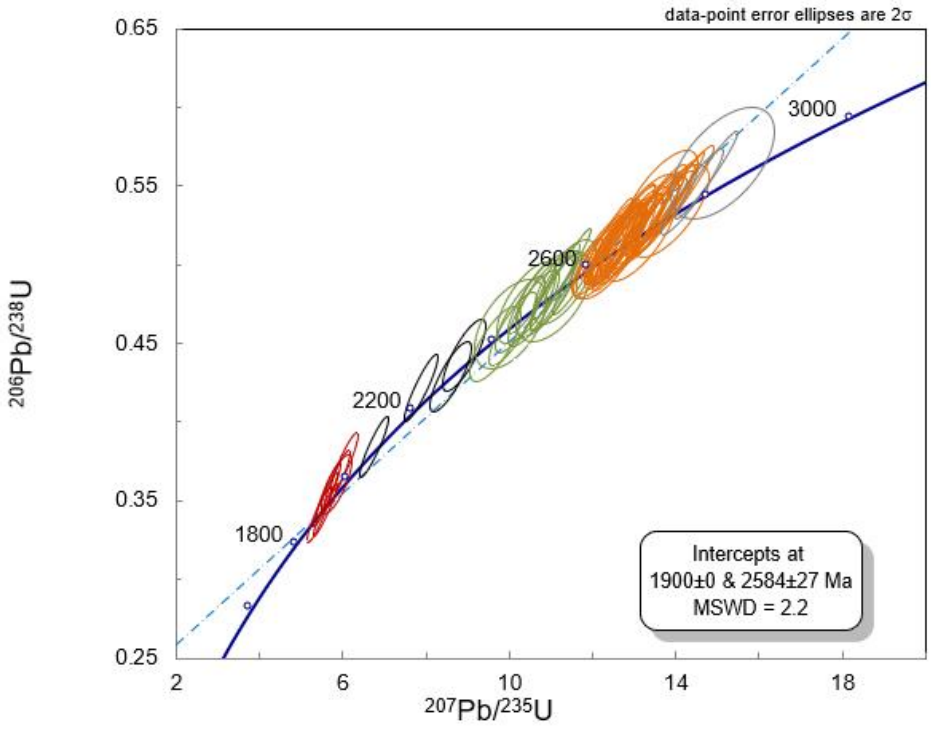

Figure 30. Upper (2584 ± 27 Ma) and lower anchored (1900 Ma) intercept ages of the plagioclase porphyry dike to demonstrate the effect of lead loss.

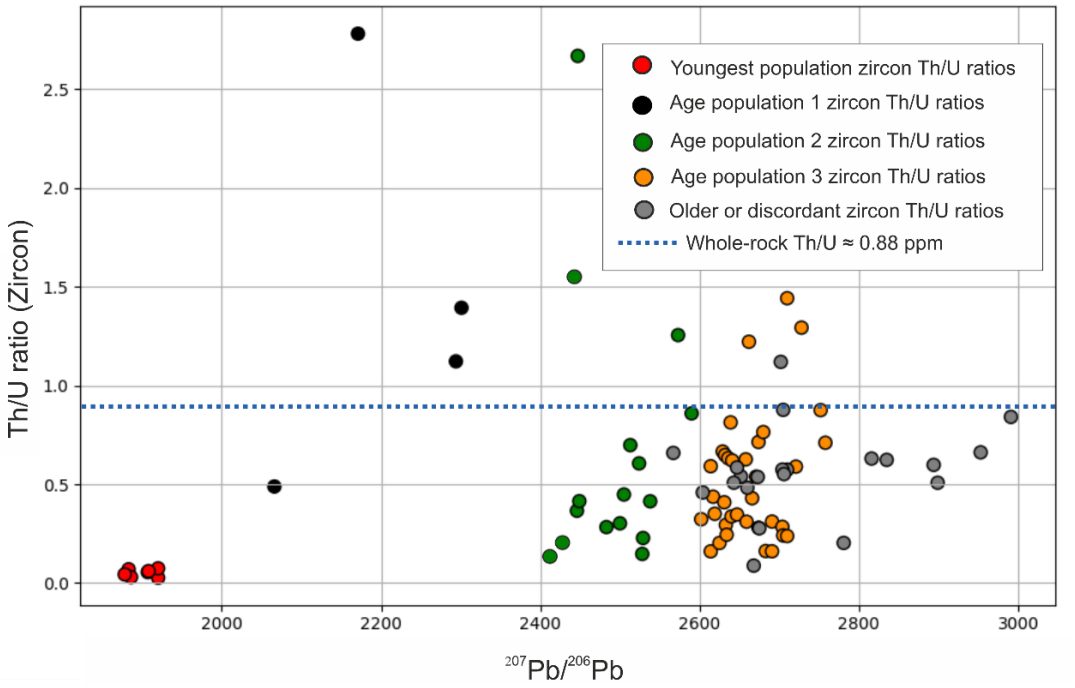

Figure 31. Th/U ratios of individual zircon analyses plotted against their corresponding $^{207}Pb/^{206}Pb$ age. A dashed blue line represents the whole rock Th/U ratio of sample EPHE-2015-301.1 for comparison. The Th concentration in the plagioclase porphyry was below the analytical detection limit (2 ppm), and for the purposes of this plot, a value of 1 ppm (half the detection limit) was used to approximate the whole-rock Th/U ratio.

The zircon dating results can be divided into five different populations (Figure 27A). The red-marked group yields concordia age that represents the youngest ages. The black-marked group, (population 1), represents younger ages, while the green population 2 indicates ages around 2.4–2.5 Ga. The orange population 3 cluster between approximately 2.5–2.7 Ga, and the gray group includes the oldest ages up to 2.9 Ga, or otherwise anomalous and slightly discordant values. Based on the ages, the location of this rock and the analysis spots which were mostly located in the core of the zircon, these older (green, orange and gray populations) ages and zircon cores are most likely inherited from the surrounding Archean basement rocks and possibly the carbonatite Complex.

Locations for all nearby published and mentioned age determinations are visible in Figure 10. Heilimo et al. (2011) has done U-Pb zircon analysis from a granodiorite augen gneiss in Nilsiä, receiving an upper intercept age of 2724 ± 28 Ma. Additionally, the U-Pb data yielded lower interception age of 1850 ± 150 Ma that was interpreted as Svecofennian episodic thermal event. Mänttäri and Hölttä (2002) have done U-Pb zircon age determination from a leucosome of a mafic granulite in Varpaisjärvi, receiving age of 2.7 Ga. The Siilinjärvi carbonatite Complex has been dated to 2609 ± 6 Ma (O'Brien et al.

2005). These ages from the surrounding crystalline rocks correspond to the ages received from the cores of the zircons.

The zircon population marked with black, yielded $^{207}Pb/^{206}Pb$ ages between 2066 and 2301 Ma, which could represent the episodic effect of lead loss (Figure 30), or alternatively zircons received from the mafic dikes or volcanites from the area (Figure 10). Kontinen et al. (1992) had analyzed a hornblende phenocrystic mafic dike (KA025) from near Koivusaari formation with K-Ar dating method from hornblende, receiving an age of 2056 ± 69 Ma, representing metamorphism after emplacement. It was interpreted that the dike is cogenetic with the Koivusaari formation volcanite. where a felsic metavolcanite has been dated with U-Pb zircon method yielding age of 2062 ± 6 Ma (Kontinen et al. 1992; Huhma et al. 2018). Multiple generations of mafic dike swarms in Finland have been documented by Vuollo and Huhma (2005). They described dike swarms in the central and eastern Karelia Province with age ranges of 2350–2450 Ma and 2250–2350 Ma. These age ranges align with U-Pb zircon ages from diabase dikes in the Tulisaari island (2295 ± 5 Ma) and Lapinlahti area (2331 ± 3 Ma) reported by Paavola (1988), suggesting these dikes could correspond to the mafic sequences. In addition, Vuollo and Huhma (2005) also characterized younger dike swarms around ca. 2200 Ma and between 1990–2130 Ma. The mafic volcanites in Siilinjärvi (see Figure 10), investigated by Kontinen et al. (1992), may represent a part of these later magmatic episodes.

6.2 Geochemical characteristics and implications

The mineral assemblages observed in the studied Muuruvesi suite sample rocks closely resemble those in the reference group quartz-diorites and tonalites from the Paavola (1988) map sheet explanation. Minerals in the reference quartz-diorites and tonalites included plagioclase, quartz and biotite, hornblende, K-feldspar and epidote. The granodiorites in that study were identified with similar main minerals and accessory minerals including epidote and chlorite. Similarly, the geochemical signatures, particularly in the TAS and major element diagrams, show that the studied three Muuruvesi suite rock sample plot either directly on or very close to the reference group rocks, suggesting they may represent cogenetic magmatic suites.

In contrast, the dated plagioclase porphyry is chemically distinct. It is characterized by large phenocrysts of Na-rich plagioclase and K-feldspar, leading to the highest amounts

of Na and K in the TAS (Figure 19) and major element diagrams (Figure 21). It exhibits elevated alkali content relative to SiO_2 compared to reference rocks as evidenced by the position in the TAS diagram (Figure 19). While it deviates from reference group rocks in most major element diagrams (except for CaO concentrations), it consistently plots between these groups (Figure 21). Plotting to the quartz monzonite field in TAS diagram however correlates to the observed mineralogy as the amount of quartz was not significant and is most likely <20 %, and the amount of plagioclase and K-feldspar was high and near equal (Streckeisen 1974).

The major element diagrams (Figure 21) support the petrographic classification, as the rock identified as Muuruvesi melatonalite has the highest concentrations in Fe and Mg, and low concentrations in K and Na which indicates more mafic composition with minimal K-feldspar. This is consistent with the dominance of biotite and hornblende. The high amount of Al and low Na_2O with highest CaO value also indicates the presence of biotite and more Ca-rich plagioclase. Chemically, the melatonalite aligns with the reference group quartz-diorites and tonalites, except for slightly lower Al and higher MgO. The minerals observed in the more mafic granodiorite are also supported by the concentrations depicted in the major element diagrams (Figure 21). The lower amount in K_2O could be due to the very minor amount of K-feldspar present. The high concentration of Al likely reflects the abundance of plagioclase, biotite, chlorite and epidote that are found from the rock. Potential sources for Na, Al and Ca concentrations could include plagioclase, biotite and epidote. Likewise, Fe and Mg concentrations could be explained by biotite-chlorite assemblage. This rock also compositionally aligns with the reference quartz-diorites and tonalites based in both TAS (Figure 19) and major elements diagrams (Figure 21) with only minor variations in the concentrations of Na_2O and MgO.

The mineralogical composition of the more felsic granodiorite of Muuruvesi suite is consistent with its major element geochemistry. Elevated K and Na concentrations (Figure 21) reflect the presence of Na-rich plagioclase and K-feldspar, while lower abundances of Al, Ca, Fe, and Mg align with its high quartz content and reduced proportions of mafic minerals (e.g., biotite) and plagioclase. This also closely matches the reference group granodiorites as it plots within the same TAS diagram field (Figure 19) and shows strong correlations in major element compositions (Figure 21). The only minor deviation is a slightly lower Al_2O_3 content compared to the reference group.

In the granite tectonic discrimination diagram (Figure 20) all the studied Muuruvesi suite plutonites and the plagioclase porphyry dike follow mainly a similar pattern as the reference group rocks. The reference group rocks are mainly magnesian as are the sample rocks, indicating higher magnesium content compared to iron. The reference quartz-diorites and tonalites plot within the calc-alkalic field (Figure 20B) along with the melatonalite and granodiorite, maintaining consistent geochemical trend across all diagrams. Likewise, the reference granodiorite group follows the plagioclase porphyry and the felsic granodiorite in the calc-alkalic and alkali-calcic fields. According to Frost et al (2001), magnesian rocks are generally calc-alkalic or calcic, and rarely alkali-calcic or alkalic, which makes the geochemical position of the plagioclase porphyry somewhat atypical. The elevated K_2O and Na_2O concentrations relative to SiO_2, and the mineralogical observations, indicate late-stage alkali-enrichment, that could explain the atypical magnesian and alkali-calcic geochemistry. In the aluminum saturation diagram (Figure 20C) the sample rocks plotted to the metaluminous field. This indicates that the rocks contain more calcium than can be incorporated into feldspars once all the available aluminum has been used (Frost et al. 2001). The excess of Ca is often incorporated into calcic phases as hornblende and augite (Frost et al. 2001), however honblende is only found from the melatonalite, but the presence of epidote-group minerals across all the rocks and calcite in the plagioclase porphyry indicates calcium crystallization into secondary phases. The reference group rocks plotting also to peraluminous field (Figure 20C) indicate additional aluminous phases as they have excess Al after the crystallization of feldspars (Frost et al. 2001).

6.3 Alterations

All of the studied sample rocks exhibit similar and noticeable alteration features, which are well observed in the thin sections. Plagioclase grains in all the samples are significantly altered. Alteration includes sericitization and saussuritization, commonly resulting in replacement by epidote-group minerals such as epidote and clinozoisite (Figure 32). Twin lamellae in plagioclase are poorly preserved, indicating recrystallization or deformation. These features suggest low-grade metamorphism that has not been sufficient to open the zircon grains. This metamorphic event must postdate the potential magmatic age of ~1900 Ma, most likely occurring during the later stages of the Svecofennian orogeny.

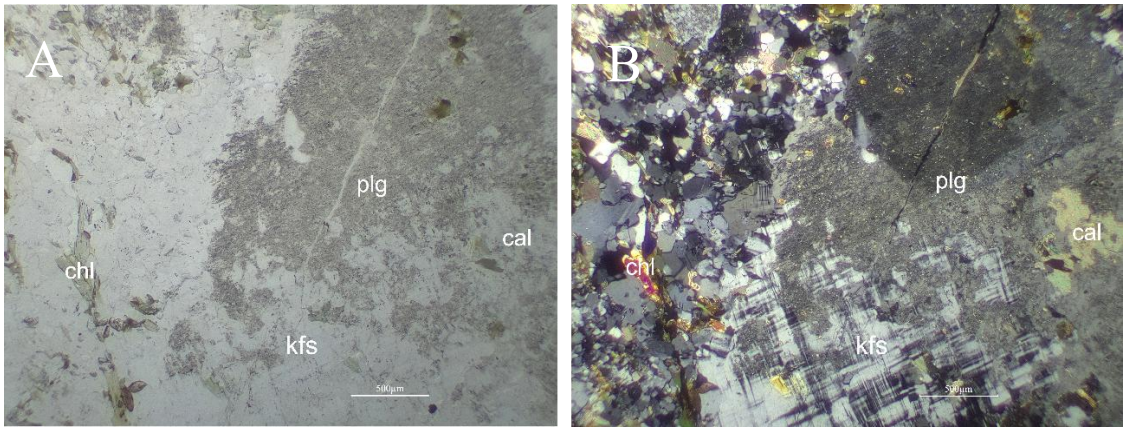

Figure 32. Plane polarized (A) and cross polarized (B) images of the plagioclase porphyry (EPHE-2015-301.1). Plagioclase porphyries (plg) and alteration to sericite, saussurite and epidote (ep) minerals. Biotite (bt) alteration to chlorite (chl) and plagioclase alteration to K-feldspar (kfs). Calcite (cal) is found in plagioclase and K-feldspar.

In the plagioclase porphyry alteration is especially notable. The plagioclase phenocrysts are partially replaced by K-feldspar and calcite occurs within or near these grains (Figure 32). The oligoclase plagioclase might have experienced albitization, leading to the release of Ca. This is then displayed as the calcite in the plagioclase grains. This suggests albitization and subsequent replacement by K-feldspar, possibly driven by alkali-rich fluids. Simplified reaction pathways are presented in equations 7 and 8 (modified after Morad et al. 2010; Yuan et al. 2019):

$$(NaCa)AlSi_3O_{8(Oligoclase)} + Na^+ + HCO_3^- \rightarrow NaAlSi_3O_{8(Albite)} + CaCO_{3(Calcite)} \quad (7)$$

$$NaAlSi_3O_{8(Albite)} + K^+ \rightarrow KAlSi_3O_{8(Microcline)} + Na^+ \quad (8)$$

These reactions (Figure 32) imply an influx of alkali (Na and K) fluids, potentially sourced from the nearby fenites. The calcite may also reflect interaction with carbonatite-derived fluids from the Siilinjärvi carbonatite Complex. Additionally, the alteration of biotite to chlorite in hydrothermal environments could provide potassium for the formation of K-feldspar. The presence of epidote-group minerals across all samples, combined with late-stage K enrichment and secondary calcite formation, points to metasomatic overprinting. The studied rock is located along a N-S trending shear zone (Figure13) which may have acted as a pathway for fluid migration. The observed compositions support Lukkarinen (2008) description of a regionally comparable lower to mid-amphibolite facies metamorphic overprint.

6.4 Implications for the geological evolution of the area

The Kuopio-Siilinjärvi area lies on the Archean rocks in Karelia Province (Figure 10). Archean rifting, possibly already initiated at 2.6–2.5 Ga, may have created the extensional setting for the Siilinjärvi carbonatite Complex (Nironen 2017). This was followed by mafic magmatism (ca. 2.3 and 2.05 Ga) and final craton breakup (~2.06 Ga), prior to the Svecofennian orogeny (1.92–1.87 Ga) which is characterized by microcontinental collisions and deformation along the Karelia-Svecofennia boundary (Lahtinen et al. 2005; Vuollo and Huhma 2005). The U-Pb age of approximately 1.9 Ga for the plagioclase porphyry places it within the Svecofennian timeframe, but its interpretation as either a primary crystallization age or a metamorphic age has different implications.

One scenario considers the 1.9 Ga age as the crystallization age of the plagioclase porphyry dike, where its emplacement would be contemporaneous with the Svecofennian collisional events. It may have provided the setting and pathways for the intrusion of magma through for example reactivated shear zones in the older carbonatite Complex. Based on field observations the plagioclase porphyry dike crosscuts the Muuruvesi suite tonalite-diorites validating it as the youngest igneous body, which would be consistent with it being a late-stage magmatic pulse during the Svecofennian orogeny. Therefore, the Muuruvesi suite rocks should represent earlier phases of Svecofennian orogeny eg. 1.93–1.91 Savo belt (Nironen 2017) or even older crustal components. Following the 1.9 Ga emplacement, both the plagioclase porphyry and the Muuruvesi suite rocks would have experienced Svecofennian overprinting and fluid activity altering them.

This interpretation is supported by the titanite, zircon and hornblende ages from similar rocks in the area. As part of the reference group rocks used in this study, Paavola (1988) described quartz-diorites and tonalites in Lapinlahti area, with similar mineralogy as the Muuruvesi suite sample rocks. However, the age determination method in the Paavola map-sheet explanation (1988) was ID-TIMS (Isotope Dilution Thermal Ionization Mass Spectrometry) which involved bulk dissolution of multiple zircon grains, resulting in mixed ages or reflecting averaged age information. This differs from the in situ analyses done in this study which resolves age variations within individual zircon grains. Despite these differences, Paavola's (1988) U-Pb data provide valuable regional context. For a quartz-diorite in Leppälahti, reported ages include a zircon age of 1902 Ma and a titanite

age of 1851 ± 82 Ma. A microtonalite from Levämäki yielded a titanite age of 1857 ± 41 Ma, alongside a mixed zircon population age between 1880 and 1924 Ma. Furthermore, for granodiorite samples from Jussilansaari, Viitasalmi, and Känninniemi, he reported an upper intercept zircon age of 1908 ± 16 Ma and a titanite age of 1874 ± 10 Ma. Paavola (1988) had interpreted the titanite ages to represent titanite closing time (~500°C) after the peak of metamorphism. From Archean rocks in eastern Finland, Kontinen et al. (1992) determined mean ages of 1851 ± 41 Ma for reset hornblendes and 1795 ± 21 Ma for reset biotites. Based on this it is assumed that the area has received heat from the Svecofennian orogeny at least over 300°C (for biotite) but also in some areas close to 500°C (for hornblende), which have been interpreted as the closing temperatures for these minerals (Kontinen et al. 1992). Therefore, the mineralogical alteration features observed in all the studied sample rocks would reflect the regional Svecofennian metamorphic overprint.

Alternatively, the 1.9 Ga age of the plagioclase porphyry could reflect a metamorphic overprint, implying its original crystallization occurred at an earlier time, potentially in the Archean or early Paleoproterozoic. If this is the case, the Svecofennian orogeny would be responsible for metamorphism of this older porphyry and the surrounding, even older, Muuruvesi suite rocks, since field relations imply they are older than the plagioclase porphyry dikes emplacement. The 1.9 Ga age from the porphyry zircons would then represent the timing of this metamorphic zircon growth or isotopic resetting. The geochronological evidence from Paavola (1988) and Kontinen et al. (1992) would verify the metamorphic overprint. However, this scenario raises challenges as Paavola (1988) interpreted ~1.9 Ga zircon ages from the reference tonalitic rocks as crystallization ages. While acknowledging that the ID-TIMS methodology might yield averaged ages not directly analogous to in situ results, the suggestion of ~1.9 Ga magmatism in rocks comparable to the Muuruvesi suite is noteworthy. If the Muuruvesi suite did crystallize around ~1.9 Ga, then the porphyry which crosscuts it must be younger. This would conflict with the metamorphic interpretation of the porphyry's 1.9 Ga age.

To better understand the geological history and solve these competing interpretations, direct U-Pb crystallization age determinations for the Muuruvesi suite tonalite-diorites are essential. These would help to clarify their relationship with the plagioclase porphyry dike and help to understand the origin and significance of the geochronological data of the dike.

7 Conclusions

- In situ U-Pb LA-ICPMS dating of zircons from the plagioclase porphyry dike in the Siilinjärvi mine area yielded a concordia age of 1900 ± 14 Ma. This age can be interpreted in two primary ways:

    - The 1900 ± 14 Ma age may represent the crystallization age of the plagioclase porphyry, suggesting emplacement during Svecofennian collisional events. This interpretation is supported by analyses of the outermost zircon rims exhibiting magmatic growth zoning.

    - Alternatively, the result may represent a Svecofennian metamorphic overprint on an older intrusion. This is supported by a discordia line with an upper intercept of 2584 ± 27 Ma and low Th/U ratios (0.026-0.072) in the youngest zircon rims, which are often characteristic of metamorphic zircons.

- Whole-rock geochemistry shows the plagioclase porphyry is chemically distinct from the Muuruvesi suite samples, characterized by higher alkali content (Na_2O+K_2O). The Muuruvesi suite samples align well with reference quartz-diorites, tonalites, and granodiorites from the region.

- All studied samples exhibit significant alteration (sericitization, saussuritization, epidote-group mineral formation, chloritization of biotite), indicative of low-grade metamorphism, likely related to the Svecofennian orogeny. The plagioclase porphyry shows additional K-feldspar replacement and calcite, possibly due to alkali-rich fluids from nearby reactivated fenites.

- Field evidence shows that the plagioclase porphyry crosscuts the Muuruvesi suite tonalite-diorites, indicating it is the youngest unit. However, this relationship is problematic if both yield similar ~1.9 Ga U-Pb ages and the porphyry's age is interpreted as metamorphic. Further research, particularly U-Pb crystallization dating of the Muuruvesi suite, is essential to clarify the temporal relationship and geological evolution of the Siilinjärvi area.

Acknowledgements

My deepest thanks go to my supervisor Professor Esa Heilimo for providing material for this research and continuous support throughout this thesis. I would also like to thank my co-supervisor University Teacher Teemu Vehkamäki for valuable guidance during the research process and providing insightful feedback. Thank you to the laboratory technician Arto Peltola for the preparation of the thin sections and the zircon mounts and researcher Ermei Mäkilä for their extensive work on the BSE and CL imaging. Special thanks also to Research Scientist Matti Kurhila from GTK for hosting the geochronological laboratory work and carrying out the data reduction.

References

Abdel Zaher, M., Pirttijärvi, M. and Korja, T. (2017). Geophysical studies of the Raahe-ladoga shear complex in the Iisalmi area of Finland. *Geophysica* 52. 43–67.

Allègre, C. (2008). *Isotope geology*. Cambridge University Press. Cambridge, UK New York. 512 p.

Boynton, W. V. (1984). Cosmochemistry of the Rare Earth Elements: Meteorite Studies. In: Henderson, P. (ed.) *Developments in Geochemistry*. Elsevier. 63–114.

Corfu, F. (2015). Uranium–Lead, Zircon. In: Jack Rink, W. and Thompson, J. W. (eds.) *Encyclopedia of Scientific Dating Methods*. Springer Netherlands, Dordrecht. 914–918.

Corfu, F., Hanchar, J. M., Hoskin, P. W. O. and Kinny, P. (2003). Atlas of Zircon Textures. In: Hanchar, J. M. and Hoskin, P. W. O. (eds). *Zircon.* 1st ed. Walter de Gruyter GmbH, Washington D.C. 469–500.

Dickin, A. P. (2018). *Radiogenic Isotope Geology*. 3rd ed. Cambridge University Press, Cambridge. 482 p.

Faure, G. (1977). *Principles of isotope geology*. Wiley, New York. 464 p.

Finch, R. J. and Hanchar, J. M. (2003). Structure and Chemistry of Zircon and Zircon-Group Minerals. In: Hanchar, J. M. and Hoskin, P. W. O. (eds.) *Zircon.* 1st ed. Walter de Gruyter GmbH, Washington D.C. 1–24.

Frost, B. R., Barnes, C. G., Collins, W. J., Arculus, R. J., Ellis, D. J. and Frost, C. D. (2001). A geochemical classification for granitic rocks. *Journal of Petrology* 42, 2033–2048.

Gaál, G. and Gorbatschev, R. (1987). An Outline of the precambrian evolution of the baltic shield. *Precambrian Geology and Evolution of the Cental Baltic Shield* 35, 15–52.

Gorbatschev, R. and Bogdanova, S. (1993). Frontiers in the Baltic Shield. *Precambrian Research* 64, 3–21.

Heilimo, E., Halla, J. and Huhma, H. (2011). Single-grain zircon U–Pb age constraints of the western and eastern sanukitoid zones in the Finnish part of the Karelian Province. *Lithos* 121, 87–99.

Hölttä, P., Heilimo, E., Huhma, H., Kontinen, A., Mertanen, S., Mikkola, P., Paavola, J., Peltonen, P., Semprich, J., Slabunov, A. and Sorjonen-Ward, P. (2012). The Archaean of the Karelia Province in Finland. *Geological Survey of Finland, Special Paper* 54, 21–73.

Hölttä, P., Huhma, H., Mänttäri, I. and Paavola, J. (2000). P–T–t development of Archaean granulites in Varpaisjärvi, Central Finland: II. Dating of high-grade metamorphism with the U–Pb and Sm–Nd methods. *Lithos* 50, 121–136.

Horstwood, M. S. A., Košler, J., Gehrels, G., Jackson, S., McLean, N., Paton, C., Pearson, N., Sircombe, K., Sylvester, P., Vermeesch, P., Bowring, J., Condon, D. and Schoene, B. (2016). Community-Derived Standards for LA-ICP-MS U-(Th-)Pb Geochronology – Uncertainty Propagation, Age Interpretation and Data Reporting. *Geostandards and Geoanalytical Research* 40, 311–332.

Hoskin, P. W. O. and Schaltegger, U. (2003). The Composition of Zircon and Igneous and Metamorphic Petrogenesis. In: Hanchar, J. M. and Hoskin, P. W. O. (eds.) *Zircon*. 1st ed. Walter de Gruyter GmbH, Washington D.C. 27–62.

Huhma, H., Hanski, E., Kontinen, A., Vuollo, J., Mänttäri, I. and Lahaye, Y. (2018). Sm–Nd and U–Pb isotope geochemistry of the Palaeoproterozoic mafic magmatism in eastern and northern Finland. *Geological Survey of Finland, Bulletin - Monograph* 405. 150 p.

Huhma, H., Mänttäri, I., Peltonen, P., Kontinen, A., Halkoaho, T., Hanski, E., Hokkanen, T., Hölttä, P., Juopperi, H., Konnunaho, J., Layahe, Y., Luukkonen. E.,

Pietikäinen. K., Pulkkinen, A., Sorjonen-Ward, P., Vaasjoki, M. and Whitehouse, M. (2012). The age of the Archaean greenstone belts in Finland. *Geological Survey of Finland, Special Paper* 54, 74−175.

Janoušek, V., Farrow, C. M. and Erban, V. (2006). Interpretation of Whole-rock Geochemical Data in Igneous Geochemistry: Introducing Geochemical Data Toolkit (GCDkit). *Journal of Petrology* 47, 1255–1259.

Jara, J. J., Barra, F., Reich, M., Morata, D., Leisen, M. and Romero, R. (2021). Geochronology and petrogenesis of intrusive rocks in the Coastal Cordillera of northern Chile: Insights from zircon U-Pb dating and trace element geochemistry. *Gondwana Research 93*, 48–72

Kirkland, C. L., Smithies, R. H., Taylor, R. J. M., Evans, N. and McDonald, B. (2015). Zircon Th/U ratios in magmatic environs. *Lithos* 212–215, 397–414.

Kontinen, A., Paavola, J. and Lukkarinen, H. (1992). K-Ar ages of hornblende and biotite from Late Archaean rocks of eastern Finland-interpretation and discussion of tectonic implications. *Geological survey of Finland, Bulletin - Bulletin de la Commission Géologique de Finlande*, 1–31.

Korja, A., Lahtinen, R. and Nironen, M. (2006). The Svecofennian orogen: a collage of microcontinents and island arcs. *Geological Society, London, Memoirs* 32, 561–578.

Kärki, A., Korja, T., Mahmoud, M., Tirronniemi, J., Tuisku, P. and Woodard, J. (2012). Structure of the Raahe –Ladoga Shear Complex. In: Kukkonen, I. et al. (eds.) *Lithosphere 2012 – Seventh Symposium on the Structure, Composition and Evolution of the Lithosphere in Finland*. Institute of Seismology, University of Helsinki, Espoo. 55–58.

Kärki, A., Laajoki, K. and Luukas, J. (1993). Major Palaeoproterozoic shear zones of the central Fennoscandian Shield. *Precambrian Research* 64, 207–223.

Laajoki, K. (2005). Karelian supracrustal rocks. In: Lehtinen, M., Nurmi, P. A. and Rämö, O. T. (eds.) *Developments in Precambrian Geology*. Elsevier. 279–341.

Lahtinen, R., Korja, A. and Nironen, M. (2005). Paleoproterozoic tectonic evolution. In: Lehtinen, M., Nurmi, P. A., and Rämö, O. T. (eds.) *Developments in Precambrian Geology*. Elsevier. 481–531.

Le Maitre, R. W., Streckeisen, A., Zanettin, B., Le Bas, M. J., Bonin, B., & Bateman, P. (2002). *Igneous rocks: A classification and glossary of terms: Recommendations of the International Union of Geological Sciences Subcommission on the Systematics of Igneous Rocks*. Cambridge University Press. 236 p.

Lukkarinen, H. (2008). *Siilinjärven ja Kuopion kartta-alueiden kallioperä. Suomengeologinen kartta - 1:100 000. Kallioperäkarttojen selitykset, lehdet 3242 ja 3331.* Geological Survey of Finland, Espoo. 228 p.

Mattsson, H. B., Högdahl, K., Carlsson, M. and Malehmir, A. (2019). The role of mafic dykes in the petrogenesis of the Archean Siilinjärvi carbonatite complex, east-central Finland. *Lithos* 342–343, 468–479.

Middlemost, E. A. K. (1994). Naming materials in the magma/igneous rock system. *Earth-Science Reviews* 37, 215–224.

Morad, S., El-Ghali, M., Caja, M. Á., Sirat, M., Al-Ramadan, K. and Mansurbeg, H. (2010). Hydrothermal alteration of plagioclase in granitic rocks from Proterozoic basement of SE Sweden. *Geological Journal* 45, 105–116.

Müller, W., Shelley, M., Miller, P. and Broude, S. (2009). Initial performance metrics of a new custom-designed ArF excimer LA-ICPMS system coupled to a two-volume laser-ablation cell. *Journal of Analytical Atomic Spectrometry* 24, 209–214.

Mänttäri, I. and Hölttä, P. (2002). U–Pb dating of zircons and monazites from Archean granulites in Varpaisjärvi, Central Finland: Evidence for multiple metamorphism and Neoarchean terrane accretion. *Precambrian Research* 118, 101–131.

Nironen, M. (2017). Bedrock of Finland at the scale 1:1 000 000 - Major stratigraphic units, metamorphism and tectonic evolution. *Geological Survey of Finland, Special Paper*. 128 p.

O'Brien, H. E., Heilimo, E. and Heino, P. (2015). The Archean Siilinjärvi Carbonatite Complex. In: Maier, W. D., Lahtinen, R. and O'Brien, H. (eds.) *Mineral Deposits of Finland*. 1st ed. Elsevier Science, Burlington. 327–343.

O'Brien, H. E., Peltonen, P. and Vartiainen, H. (2005). Kimberlites, Carbonatites, and alkaline rocks. In: Lehtinen, M., Nurmi, P. A., and Rämö, O. T. (eds.) *Developments in Precambrian Geology*. Elsevier. 605–644.

Paavola, J. (1988*). Lapinlahden kartta-alueen kallioperä. Geological map of Finland 1 : 100 000. Pre-Quaternary rocks of the Lapinlahti map-sheet area, Sheet 3332*. Geologial Survey of Finland, Espoo. 60 p.

Puustinen, K. (1969). The carbonatite of Siilinjärvi in the precambrian of Eastern Finland: A preliminary report. *Lithos* 3, 89–92.

Puustinen, K. (1971). Geology of the Siilinjärvi Carbonatite Complex, Eastern Finland. *Bulletin de la Commission Géologique de Finlande* 249. 43 p.

Reiners, P., Carlson, R., Renne, P., Cooper, K., Granger, D., McLean, N. and Schoene, B. (2017). *Geochronology and Thermochronology*. John Wiley & Sons. 491 p.

Schoene, B. (2013). U-Th-Pb geochronology. In: Holland, H. D. and Turekian, K.K. (eds.) *Treatise on Geochemistry*: Second Edition 4. 341–378.

Shand, S. J. (1943). *Eruptive Rocks. Their Genesis, Composition, Classification, and Their Relation to Ore-Deposits with a Chapter on Meteorite*. John Wiley & Sons, New York. 444 p.

Sorjonen-Ward, P. and Luukkonen, E. J. (2005). Archean rocks. In: Lehtinen, M., Nurmi, P. A. and Rämö, O. T. (eds.) *Developments in Precambrian Geology*. Elsevier. 19–99.

Speer, J. A. (1982). Zircon. In: Ribbe, P. H. (ed.) *Orthosilicates. Reviews in Mineralogy* 5. Mineralogical Society of America, 67–112.

Sun S. S. and McDonough W. (1989). Chemical and isotopic systematics of oceanic basalts: implications for mantle composition and processes. *Geological Society of London, special publication* 42, 313–345.

Tichomirowa, M., Whitehouse, M. J., Gerdes, A., Götze, J., Schulz, B. and Belyatsky, B. V. (2013). Different zircon recrystallization types in carbonatites caused by magma mixing: Evidence from U–Pb dating, trace element and isotope composition (Hf and O) of zircons from two Precambrian carbonatites from Fennoscandia. *Chemical Geology* 353, 173–198.

Vaasjoki, M., Korsman, K. and Koistinen, T. (2005). Overview. In: Lehtinen, M., Nurmi, P. A., and Rämö, O. T. (eds.) *Developments in Precambrian Geology*. Elsevier. 1–17.

Van Achterbergh, E., Ryan C., Jackson, S. and Griffin W. (2001). Data reduction software for LA-ICP-MS, in: Sylverster P. (Ed.) *Laser-Ablation ICPMS in the Earth Sciences – Principles and applications, Mineralogical Association of Canada short course series* 29. St John, Newfoundland. 239–243.

Vuollo, J. and Huhma, H. (2005). Paleoproterozoic mafic dikes in NE Finland. In: Lehtinen, M., Nurmi, P. A., and Rämö, O. T. (eds.) *Developments in Precambrian Geology*. Elsevier. 195–236.

Yakymchuk, C., Kirkland, C.L. and Clark, C. (2018). Th/U ratios in metamorphic zircon. *Journal of Metamorphic Geology* 36, 715–737.

Yuan, G., Cao, Y., Schulz, H., Hao, F., Gluyas, J., Liu, K. Yang, T., Wang, Y., Xi, K. and Li, F. (2019). A review of feldspar alteration and its geological significance in sedimentary basins: From shallow aquifers to deep hydrocarbon reservoirs. *Earth-Science Reviews* 191, 114–140.

Appendices

Appendix 1. Coordinates of the rock samples. Coordinates are given in ETRS-TM35FIN system.

Sample ID	Rock type	North	East	Elevation
EPHE-2015-300.1	Melatonalite	6997852	536840	81
EPHE-2015-300.2	Granodiorite	6998984	536618	108
EPHE-2015-301.1	Plagioclase porphyry	6998865	536597	97
EPHE-2015-303.1	Granodiorite	6997412	536815	105

Appendix 2. Geochemical analysis data of the samples.

Unit	%	%	%	%	%	%	%	%	%	%	%	ppm	%	%
Sample ID	SiO2	Al2O3	Fe2O3	CaO	MgO	Na2O	K2O	TiO2	MnO	P2O5	As	Ba	Bi	Ga
EPHE-2015-300.1	56.17	15.95	7.5	6.71	4.22	3.88	1.521	0.855	0.107	0.37	<0.001	690	<0.003	<0.003
EPHE-2015-300.2	64.42	16.29	5.08	4.15	1.46	5.0	1.53	0.55	0.059	0.221	<0.001	1110	<0.003	<0.003
EPHE-2015-301.1	63.22	15.77	3.27	3.73	1.65	5.5	3.344	0.302	0.055	0.156	<0.001	870	<0.003	<0.003
EPHE-2015-303.1	71.84	13.5	2.47	1.88	1.04	4.63	2.942	0.23	0.028	0.087	<0.001	1070	<0.003	<0.003

Unit	ppm	%	ppm	%	%	ppm	ppm	ppm	ppm	ppm	ppm	ppm	ppm	%
Sample ID	Ce	Cl	Co	Cr	Cu	Dy	Er	Eu	Gd	Hf	Ho	La	Lu	Mo
EPHE-2015-300.1	62.1	0.02	21.3	0.01	0.002	2.88	1.56	1.51	3.98	3.77	0.56	31.5	0.21	<0.001
EPHE-2015-300.2	222.0	0.03	9.73	0.003	<0.002	3.02	1.65	2.0	5.79	7.29	0.56	130.0	0.24	<0.001
EPHE-2015-301.1	22.6	0.02	9.55	0.005	0.003	1.5	0.9	0.77	1.87	2.65	0.3	11.4	0.14	<0.001
EPHE-2015-303.1	85.0	0.02	5.34	0.002	<0.002	1.85	1.0	1.1	3.07	3.83	0.35	47.7	0.15	<0.001

Unit	ppm	ppm	%	%	ppm	ppm	%	%	ppm	ppm	%	%	ppm	ppm
Sample ID	Nb	Nd	Ni	Pb	Pr	Rb	S	Sb	Sc	Sm	Sn	Sr	Ta	Tb
EPHE-2015-300.1	8.36	27.7	0.005	<0.003	7.37	25.9	0.04	<0.005	16.7	4.81	<0.003	0.072	<1	0.53
EPHE-2015-300.2	11.3	67.0	0.003	0.003	21.3	28.8	0.01	<0.005	6.0	8.12	<0.003	0.076	<1	0.63
EPHE-2015-301.1	7.74	10.9	0.004	0.004	2.73	60.2	0.05	<0.005	6.5	2.18	<0.003	0.067	<1	0.25
EPHE-2015-303.1	8.1	29.3	0.003	0.004	8.79	45.1	<0.001	<0.005	2.6	4.15	<0.003	0.039	<1	0.37

Unit	ppm	ppm	ppm	ppm	ppm	ppm	%	ppm
Sample ID	Th	Tm	U	V	Y	Yb	Zn	Zr
EPHE-2015-300.1	2.9	0.21	3.99	109.0	14.2	1.34	0.009	117
EPHE-2015-300.2	8.55	0.22	1.38	25.9	14.6	1.44	0.009	326
EPHE-2015-301.1	<2	0.12	1.14	29.5	7.88	0.84	0.004	91
EPHE-2015-303.1	5.77	0.14	1.67	10.4	9.4	0.94	0.005	145

Appendix 3. U-Pb data of age determination of the plagioclase porphyry dike.

Plagioclase porphyry																									
Sample	comment	Pb206/Pb204	206Pbc(%)	Pb	Th	U	Th/U	Ratios												Ages					
				ppm				207Pb/206Pb	1s	207Pb/235U	1s	206Pb/238U	1s	r	% Concordance	207Pb/206Pb	1s	207Pb/235U	1s	206Pb/238U	1s
Nappl2_14b		658016	0.0026	130	24	351	0.0695	0.1152	0.0008	5.567	0.117	0.350	0.007	0.95	103	1883	12	1937	34	1937	33
Nappl2_12c		266474	0.0065	52	4	146	0.0300	0.1154	0.0010	5.416	0.117	0.341	0.007	0.92	100	1886	16	1887	33	1889	33
Nappl2_20b		182468	0.0094	36	3	98	0.0267	0.1176	0.0009	5.583	0.117	0.344	0.007	0.95	99	1920	12	1913	33	1907	33
Nappl1_07b		20521	0.0839	93	13	235	0.0552	0.1167	0.0010	5.864	0.126	0.364	0.007	0.92	105	1907	15	1956	19	2003	35
Nappl2_31		602467	0.0029	119	14	316	0.0438	0.1149	0.0009	5.655	0.121	0.357	0.007	0.93	105	1878	15	1925	18	1968	34
Nappl1_01c	end of run	216240	0.0080	43	8	108	0.0742	0.1176	0.0019	5.842	0.146	0.360	0.008	0.78	103	1920	28	1953	21	1984	36
Nappl2_35b		540287	0.0032	107	16	270	0.0604	0.1168	0.0011	6.033	0.151	0.375	0.008	0.91	107	1908	16	1981	19	2051	35
Nappl2_07		176747	0.0097	39	42	86	0.4886	0.1277	0.0011	6.758	0.145	0.384	0.008	0.92	102	2066	15	2080	19	2095	36
Nappl1_12b		50002	0.0344	17	61	22	2.7819	0.1356	0.0012	7.881	0.170	0.422	0.009	0.91	104	2171	15	2217	19	2268	39
Nappl2_04b		38752	0.0444	10	19	17	1.1225	0.1455	0.0020	8.608	0.204	0.429	0.009	0.82	100	2294	23	2397	21	2391	41
Nappl1_12a		23808	0.0723	6	14	10	1.3938	0.1462	0.0021	8.920	0.215	0.443	0.009	0.81	103	2301	24	2330	22	2362	42
Nappl2_32b		13707	0.1256	3	1	6	0.1344	0.1559	0.0027	9.671	0.248	0.450	0.010	0.75	99	2412	29	2404	23	2395	43
Nappl1_08b		7687	0.2239	2	1	3	0.2047	0.1574	0.0047	10.033	0.347	0.462	0.011	0.54	101	2428	50	2438	31	2450	50
Nappl1_11		49589	0.0347	14	29	19	1.5507	0.1588	0.0032	10.416	0.287	0.476	0.011	0.70	103	2443	33	2473	25	2509	46
Nappl1_01b		18243	0.0944	4	3	7	0.3660	0.1591	0.0022	10.271	0.243	0.468	0.010	0.82	101	2446	23	2459	22	2476	43
Nappl2_33a		71490	0.0241	24	78	29	2.6693	0.1592	0.0020	10.078	0.235	0.459	0.010	0.84	100	2447	21	2442	21	2436	42
Nappl2_05a		109206	0.0158	24	17	42	0.4146	0.1593	0.0015	10.542	0.231	0.480	0.010	0.90	103	2449	16	2484	20	2526	43
Nappl2_10b		51626	0.0333	11	6	20	0.2831	0.1626	0.0022	10.594	0.251	0.473	0.010	0.82	100	2483	23	2488	22	2495	44
Nappl1_09b		43531	0.0395	10	5	17	0.3022	0.1643	0.0028	10.859	0.278	0.479	0.010	0.75	101	2500	28	2511	24	2525	45
Nappl2_11		294400	0.0058	67	50	112	0.4481	0.1647	0.0013	10.416	0.236	0.489	0.010	0.93	102	2505	13	2532	20	2567	43
Nappl2_26a		347339	0.0050	82	90	129	0.6982	0.1656	0.0009	11.373	0.233	0.498	0.010	0.97	104	2513	9	2554	19	2606	43
Nappl2_30a		438101	0.0039	101	101	166	0.6058	0.1666	0.0014	11.088	0.238	0.483	0.010	0.92	101	2524	14	2531	20	2538	42
Nappl2_32	low Pb	4722	0.3646	1	0	2	0.1472	0.1670	0.0047	11.058	0.371	0.480	0.012	0.56	100	2528	47	2528	31	2528	51
Nappl2_15a		109863	0.0157	24	10	42	0.2279	0.1671	0.0018	11.132	0.249	0.483	0.010	0.88	100	2529	18	2534	21	2540	43
Nappl1_15b		18953	0.0908	4	3	7	0.4139	0.1680	0.0033	11.329	0.309	0.489	0.011	0.70	101	2538	33	2551	25	2567	47
Nappl2_15c		458590	0.0038	123	219	174	1.2554	0.1716	0.0012	11.647	0.245	0.492	0.010	0.94	100	2573	12	2576	20	2581	43
Nappl1_01a		206872	0.0083	51	63	73	0.8590	0.1733	0.0010	12.344	0.254	0.517	0.010	0.96	104	2590	9	2631	19	2684	44
Nappl2_30b		26873	0.0641	6	3	10	0.3230	0.1746	0.0022	12.189	0.282	0.506	0.011	0.85	101	2602	21	2619	21	2641	45
Nappl2_25		165274	0.0104	39	35	60	0.5914	0.1759	0.0018	12.488	0.277	0.515	0.011	0.89	102	2614	17	2642	21	2678	45
Nappl2_22a		425767	0.0040	91	25	154	0.1602	0.1759	0.0010	12.516	0.259	0.516	0.010	0.96	102	2614	10	2644	20	2683	44
Nappl2_20a		170688	0.0101	39	27	62	0.4368	0.1762	0.0015	12.464	0.267	0.513	0.010	0.92	102	2617	14	2640	20	2670	44
Nappl2_22b		27202	0.0633	6	4	10	0.3505	0.1764	0.0025	12.263	0.295	0.504	0.011	0.81	101	2619	23	2625	22	2652	46
Nappl2_22b		482244	0.0036	104	36	175	0.2028	0.1770	0.0012	12.530	0.263	0.513	0.010	0.94	102	2625	12	2645	20	2671	44
Nappl1_16		104441	0.0185	25	24	36	0.6658	0.1774	0.0013	12.843	0.271	0.525	0.011	0.94	103	2629	12	2668	20	2721	45
Nappl2_29b		224933	0.0077	51	34	83	0.4088	0.1777	0.0020	12.498	0.283	0.510	0.011	0.87	101	2631	19	2643	21	2657	45
Nappl2_19a		14562	0.1182	4	3	5	0.6479	0.1777	0.0031	12.400	0.323	0.506	0.011	0.74	100	2632	29	2635	24	2640	48
Nappl1_09a		111005	0.0155	24	12	40	0.2944	0.1778	0.0020	12.570	0.283	0.513	0.011	0.87	101	2633	18	2648	21	2678	45
Nappl2_13b		71669	0.0240	16	6	25	0.2446	0.1780	0.0016	12.639	0.274	0.515	0.011	0.91	102	2634	15	2653	20	2678	45
Nappl1_10a		180719	0.0095	43	42	66	0.6321	0.1781	0.0016	12.611	0.272	0.513	0.011	0.91	101	2636	15	2651	20	2671	45
Nappl2_13a		446634	0.0039	99	55	162	0.3371	0.1785	0.0018	12.882	0.285	0.523	0.011	0.89	103	2639	17	2671	21	2714	46
Nappl1_08a		145689	0.0118	34	32	51	0.6205	0.1786	0.0016	12.646	0.274	0.513	0.010	0.91	101	2640	15	2654	20	2671	44
Nappl2_15b		268716	0.0064	60	34	98	0.3467	0.1794	0.0011	12.658	0.263	0.512	0.010	0.95	101	2647	10	2655	19	2664	44
Nappl2_14a		298383	0.0058	71	69	109	0.6083	0.1806	0.0015	12.659	0.273	0.508	0.010	0.92	100	2658	14	2655	21	2650	44
Nappl2_09c		24557	0.0701	5	3	9	0.3105	0.1806	0.0021	12.787	0.292	0.513	0.011	0.86	100	2659	20	2664	21	2671	46
Nappl2_04a		25646	0.0671	7	11	9	1.2219	0.1809	0.0024	12.930	0.304	0.518	0.011	0.83	101	2662	22	2675	22	2692	46
Nappl1_04b		34512	0.0499	8	5	12	0.4293	0.1814	0.0031	13.234	0.340	0.529	0.012	0.76	103	2666	28	2696	24	2738	49
Nappl2_21		219288	0.0079	51	42	78	0.5386	0.1820	0.0019	13.112	0.291	0.523	0.011	0.89	101	2671	17	2688	21	2710	45
Nappl1_04a	end of run	87617	0.0196	21	21	29	0.7141	0.1823	0.0035	13.640	0.368	0.543	0.012	0.72	104	2674	31	2725	25	2794	50
Nappl2_18b		244690	0.0070	54	24	86	0.2801	0.1824	0.0014	13.374	0.283	0.532	0.011	0.94	103	2674	12	2706	20	2749	46
Nappl2_29a		472102	0.0036	116	126	164	0.7643	0.1829	0.0017	13.530	0.294	0.536	0.011	0.91	103	2680	15	2717	20	2769	46
Nappl2_18a		1271004	0.0014	273	74	455	0.1617	0.1833	0.0010	13.139	0.270	0.520	0.010	0.97	101	2683	9	2690	19	2699	44
Nappl2_09a		35157	0.0490	8	4	13	0.3111	0.1842	0.0033	13.143	0.342	0.517	0.011	0.74	102	2691	29	2690	24	2689	48
Nappl2_17b		402000	0.0043	86	23	141	0.1605	0.1842	0.0014	13.487	0.285	0.531	0.011	0.94	102	2691	12	2714	20	2746	45
Nappl2_17a		390470	0.0044	86	38	132	0.2843	0.1856	0.0012	13.746	0.286	0.537	0.011	0.95	102	2704	10	2732	19	2771	45
Nappl2_27		522844	0.0033	108	2	185	0.0100	0.1857	0.0014	13.545	0.288	0.529	0.011	0.93	101	2704	13	2718	20	2737	45
Nappl1_06b		533727	0.0032	117	44	184	0.2409	0.1858	0.0013	13.822	0.291	0.540	0.011	0.94	103	2705	12	2738	20	2772	45
Nappl1_08c		26207	0.0657	161	59	248	0.2380	0.1863	0.0008	13.999	0.284	0.545	0.011	0.98	103	2710	7	2750	19	2804	46
Nappl2_08	rising signal	201605	0.0085	55	99	69	1.4422	0.1864	0.0015	13.687	0.292	0.533	0.011	0.93	102	2710	13	2728	20	2752	45
Nappl1_03b		85859	0.0200	20	17	29	0.5894	0.1876	0.0013	14.192	0.297	0.549	0.011	0.95	104	2721	11	2763	20	2820	46
Nappl2_19b		24330	0.0708	7	11	9	1.2932	0.1884	0.0036	13.872	0.374	0.534	0.012	0.72	101	2728	31	2741	25	2758	50
Nappl2_06a		236241	0.0073	59	69	78	0.8754	0.1912	0.0014	14.404	0.304	0.546	0.011	0.94	102	2752	12	2777	20	2810	46
Nappl1_06		478632	0.0036	117	112	158	0.7103	0.1919	0.0010	14.737	0.303	0.557	0.011	0.97	103	2758	9	2798	19	2854	46
Nappl2_12a		10545	0.1632	2	1	3	0.2031	0.1945	0.0056	15.137	0.510	0.564	0.014	0.56	104	2781	46	2824	32	2885	59
Nappl1_15a		71563	0.0241	17	15	23	0.6502	0.1987	0.0017	15.438	0.333	0.563	0.012	0.92	102	2816	14	2843	20	2881	48
Nappl1_02a		612472	0.0028	147	112	187	0.5982	0.2085	0.0010	17.186	0.351	0.598	0.012	0.97	104	2894	7	2945	19	3003	48
Nappl1_02b		124493	0.0138	30	25	38	0.6617	0.2163	0.0013	17.953	0.372	0.602	0.012	0.96	103	2953	10	2987	19	3038	49
Nappl1_02c		120505	0.0143	30	31	37	0.8411	0.2214	0.0028	17.999	0.420	0.590	0.012	0.84	100	2991	20	2990	22	2988	50
Nappl2_03		375772	0.0046	83	36	129	0.2771	0.1824	0.0016	13.698	0.295	0.545	0.011	0.92	105	2675	14	2729	20	2802	46

Appendix 3.

Plagioclase porphyry																					
Sample	comment	Pb206/Pb204	206Pbc(%)	ppm			Ratios						% Concordance		Ages						
				Pb	Th	U	Th/U	207Pb/206Pb	1s	207Pb/235U	1s	206Pb/238U	1s	r	207Pb/206Pb	1s	207Pb/235U	1s	206Pb/238U	1s	
Nappi_03a	rising signal	20447	0.0842	104	75	155	0.4824	0.1808	0.0011	13.489	0.279	0.541	0.011	0.96	105	2660	10	2715	19	2789	46
Nappi_01b	0	179734	0.0096	42	33	61	0.5370	0.1822	0.0010	13.702	0.282	0.545	0.011	0.97	105	2673	9	2729	19	2806	46
Nappi_17	0	181542	0.0095	43	28	55	0.5077	0.2092	0.0011	17.467	0.358	0.606	0.012	0.97	105	2899	8	2961	20	3052	49
Nappi_26b	rising signal	57604	0.0299	14	14	21	0.6588	0.1710	0.0029	12.282	0.314	0.521	0.011	0.76	105	2567	28	2626	24	2703	48
Nappi_07a	0	28983	0.0594	103	82	143	0.5740	0.1863	0.0008	14.326	0.291	0.558	0.011	0.98	105	2710	7	2772	19	2857	46
Nappi_18b	0	106269	0.0162	25	19	36	0.5396	0.1799	0.0011	13.599	0.283	0.548	0.011	0.95	106	2652	10	2722	19	2818	46
Nappi_13	0	220502	0.0078	52	43	74	0.5851	0.1794	0.0015	13.677	0.292	0.553	0.011	0.92	107	2647	13	2728	20	2837	47
Nappi_05b	uneven	263927	0.0065	61	41	90	0.4585	0.1747	0.0011	13.101	0.273	0.544	0.011	0.95	108	2604	11	2687	19	2799	46
Nappi_14	0	13276	0.1297	81	110	98	1.1198	0.1855	0.0008	14.617	0.298	0.572	0.011	0.97	108	2702	7	2791	19	2915	47
Nappi_05a	0	195061	0.0088	46	33	65	0.5079	0.1790	0.0015	13.781	0.296	0.558	0.011	0.92	108	2643	14	2735	20	2860	47
Nappi_24	uneven	639377	0.0027	134	18	204	0.0880	0.1817	0.0014	14.178	0.303	0.566	0.011	0.93	108	2668	13	2762	20	2891	47
Nappi_28	uneven ratios	545476	0.0032	131	103	165	0.6236	0.2010	0.0010	16.931	0.348	0.611	0.012	0.97	108	2835	8	2931	19	3073	49
Nappi_05b	0	219483	0.0078	52	40	70	0.5743	0.1856	0.0009	14.752	0.302	0.576	0.012	0.97	109	2704	8	2799	19	2934	47
Nappi_18a	0	218728	0.0079	56	61	70	0.8767	0.1858	0.0017	14.990	0.326	0.585	0.012	0.91	110	2705	15	2815	20	2970	49
Nappi_01a	0	577064	0.0030	136	95	173	0.5515	0.1859	0.0011	15.502	0.321	0.605	0.012	0.96	113	2706	10	2847	20	3049	49